

1 **Source-Resolved Volatility and Oxidation State Decoupling in**  
2 **Wintertime Organic Aerosols in Seoul**

3  
4 Hwajin Kim<sup>1,2,\*</sup>, Jiwoo Jeong<sup>1</sup>, Jihye Moon<sup>1</sup>, Hyun Gu Kang<sup>2,3</sup>

5 <sup>1</sup>Department of Environmental Health Sciences, Graduate School of Public Health, Seoul National University, 08826 Seoul,  
6 South Korea

7 <sup>2</sup>Institute of Health and Environment, Graduate School of Public Health, Seoul National University, 08826 Seoul, South Korea

8 <sup>3</sup>Now at Multiphase Chemistry Department, Max Planck Institute for Chemistry, 55128 Mainz, Germany

9 *Correspondence to:* Hwajin Kim (khj0116@snu.ac.kr)

10 **Abstract.**

11 Organic aerosols (OA) are key components of wintertime urban haze, but the relationship between their oxidation  
12 state and volatility—critical for understanding aerosol evolution and improving model predictions—remains poorly  
13 constrained. While oxidation–volatility decoupling has been observed in laboratory studies, field-based evidence  
14 under real-world conditions is scarce, particularly during severe haze episodes. This study presents a field-based  
15 investigation of OA sources and their volatility characteristics in Seoul during a winter haze period, using a  
16 thermodenuder coupled with a high-resolution time-of-flight aerosol mass spectrometer (HR-ToF-AMS).

17 Positive matrix factorization resolved six OA factors: hydrocarbon-like OA, cooking, biomass burning, nitrogen-  
18 containing OA (NOA), less-oxidized oxygenated OA (LO-OOA), and more-oxidized OOA (MO-OOA). Despite  
19 having the highest oxygen-to-carbon ratio (~1.15), MO-OOA exhibited unexpectedly high volatility, indicating a  
20 decoupling between oxidation state and volatility. We attribute this to fragmentation-driven aging and autoxidation  
21 under stagnant conditions with limited OH exposure. In contrast, LO-OOA showed lower volatility and more  
22 typical oxidative behavior.

23 Additionally, NOA—a rarely resolved factor in wintertime field studies—was prominent during cold, humid, and  
24 stagnant conditions and exhibited chemical and volatility features similar to biomass burning OA, suggesting a  
25 shared combustion origin and meteorological sensitivity.

26 These findings provide one of the few field-based demonstrations of oxidation–volatility decoupling in ambient  
27 OA and highlight how source-specific properties and meteorology influence OA evolution. The results underscore  
28 the need to refine OA representation in chemical transport models, especially under haze conditions.

29 **Keywords:** Organic aerosol volatility, HR-ToF-AMS, Thermodenuder, elemental ratios, aging, fragmentation

30 **1 Introduction**

31 Atmospheric aerosols affect both human health and the environment by reducing visibility (Ghim et al., 2005; Zhao  
32 et al., 2013) and contributing to cardiovascular and respiratory diseases (Hamanaka et al., 2018; Manalisidis et al.,  
33 2020). In addition, aerosols play a significant role in climate change by scattering or absorbing solar radiation and  
34 modifying cloud properties (IPCC AR6). Among the various aerosol components—including sulfate, nitrate,  
35 ammonium, chloride, crustal materials, and water—organic aerosols (OA) are particularly important to characterize,  
36 as they account for 20–90% of submicron particulate matter (Zhang et al., 2007). Identifying OA sources and  
37 understanding their behavior are critical for effective air quality management; however, this is particularly  
38 challenging due to the vast diversity and dynamic nature of OA compounds, which originate from both natural and  
39 anthropogenic sources. Unlike inorganic aerosols, organic aerosols (OAs) evolve continuously through complex  
40 atmospheric reactions, influenced by emission sources, meteorological conditions, and aerosol properties (Jimenez  
41 et al., 2009; Hallquist et al., 2009; Robinson et al., 2007; Donahue et al., 2006; Ng et al., 2010; Cappa and Jimenez,  
42 2010).

43 Volatility is a key parameter for characterizing organic aerosol (OA) properties, as it governs gas-to-particle  
44 partitioning behavior and directly influences particle formation yields (Sinha et al., 2023). The classification of OA  
45 species based on their volatility—from extremely low-volatility (ELVOC) to semi-volatile (SVOC) and  
46 intermediate-volatility (IVOC) compounds—is central to the conceptual framework of secondary OA (SOA)  
47 formation and growth (Donahue et al., 2006). It also affects atmospheric lifetimes and human exposure by  
48 determining how long aerosols remain suspended in the atmosphere (Glasius and Goldstein, 2016). Therefore,  
49 accurately capturing OA volatility is essential for improving predictions of OA concentrations and their  
50 environmental and health impacts. However, chemical transport models often significantly underestimate OA mass  
51 compared to observations (Matsui et al., 2009; Jiang et al., 2012; Li et al., 2017), largely due to incomplete  
52 precursor inventories and simplified treatment of processes affecting OA volatility. For instance, aging—through  
53 oxidation reactions such as functionalization and fragmentation—can significantly alter volatility by changing OA  
54 chemical structure (Robinson et al., 2007; Zhao et al., 2016). Early volatility studies primarily utilized thermal  
55 denuders (TD) coupled with various detection instruments to investigate the thermal properties of bulk OA  
56 (Huffman et al., 2008). The subsequent coupling of TD with the Aerosol Mass Spectrometer allowed for  
57 component-resolved volatility measurements, providing critical, quantitative insight into the properties of OA  
58 factors (e.g., SV-OOA vs. LV-OOA) across different regions (Paciga et al., 2016; Cappa and Jimenez, 2010). These  
59 component-resolved volatility data are often used to constrain the Volatility Basis Set (VBS)—the current state-of-

60 the-art framework for modeling OA partitioning and evolution (Donahue et al., 2006). However, a limitation in  
61 many field studies is that the TD-AMS thermogram data are rarely translated into quantitative VBS distributions  
62 for individual OA factors, which limits their direct use in chemical transport models. Furthermore, the volatility of  
63 OOA during extreme haze conditions, where the expected inverse correlation between oxidation (O:C) and  
64 volatility can break down (Jimenez et al., 2009), remains poorly characterized, particularly in East Asia's highly  
65 polluted winter environments. A recent study in Korea further highlighted the importance of accounting for such  
66 processes when interpreting OA volatility under ambient conditions (Kang et al., 2022). Given its central role in  
67 OA formation, reaction, and atmospheric persistence, volatility analysis is critical for bridging the gap between  
68 measurements and model performance.

69 Traditionally, due to the complexity and variability of OA, the oxygen-to-carbon (O:C) ratio has been used as a  
70 proxy for estimating volatility. In general, higher O:C values indicate greater oxidation and lower volatility  
71 (Jimenez et al., 2009). Accordingly, many field studies classify oxygenated OA (OOA) into semi-volatile OOA  
72 (SV-OOA) and low-volatility OOA (LV-OOA) based on their O:C ratios (Ng et al., 2010; Huang et al., 2010; Mohr  
73 et al., 2012). However, this relationship is not always straightforward. Fragmentation during oxidation can increase  
74 both O:C and volatility simultaneously, disrupting the expected inverse correlation (Jimenez et al., 2009). In  
75 laboratory experiments, yields of highly oxidized SOA have been observed to decrease due to fragmentation (Xu  
76 et al., 2014; Grieshop et al., 2009). These findings suggest that while O:C can offer useful insights, it is insufficient  
77 alone to represent OA volatility. Direct volatility measurements, especially when paired with chemical composition  
78 data, are necessary to improve our understanding of OA sources and aging processes.

79 In this study, we investigate the sources and volatility characteristics of OA in Seoul during winter. Wintertime OA  
80 presents additional challenges due to its high complexity. During winter, emissions from combustion sources such  
81 as biomass burning and residential heating significantly increase, contributing large amounts of primary OA (Kim  
82 et al., 2017). Meanwhile, low ambient temperatures and reduced photochemical activity affect the formation and  
83 evolution of secondary OA (SOA). Frequent haze events further complicate the aerosol properties by extending  
84 aging times and increasing particle loadings. These overlapping sources and atmospheric conditions make winter  
85 OA particularly difficult to characterize and predict. Despite Seoul's significance for air quality management,  
86 comprehensive studies on OA volatility during winter remain limited. To address these goals, we conducted real-  
87 time, high-resolution measurements using a high-resolution time-of-flight aerosol mass spectrometer (HR-ToF-  
88 AMS) coupled with a thermodenuder (TD). The objectives of this study are to: (1) improve the understanding of

89 wintertime OA in Seoul, (2) characterize the volatility of OA associated with different sources, and (3) explore the  
90 relationship between OA volatility and chemical composition.

91 **2 Experimental methods**

92 **2.1 Sampling Site and Measurement Period**

93 We conducted continuous real-time measurements in Seoul, South Korea, from 28 November to 28 December 2019.  
94 The sampling site was located in the northeastern part of the city ( $37.60^{\circ}$  N,  $127.05^{\circ}$  E), approximately 7 km from  
95 the city center, surrounded by major roadways and mixed commercial–residential land use. Air samples were  
96 collected at an elevation of approximately 60 meters above sea level, on the fifth floor of a building. A detailed site  
97 description has been reported previously for winter Seoul (Kim et al., 2017). During this period, the average  
98 ambient temperature was  $1.76 \pm 4.3^{\circ}$  C, and the average relative humidity (RH) was  $56.9 \pm 17.5\%$ , based on data  
99 from the Korea Meteorological Administration (<http://www.kma.go.kr>).

100 **2.2 Instrumentation and Measurements**

101 The physico-chemical properties of non-refractory  $PM_1$  (NR- $PM_1$ ) species—including sulfate, nitrate, ammonium,  
102 chloride, and organics—were measured using an Aerodyne high-resolution time-of-flight aerosol mass  
103 spectrometer (HR-ToF-AMS) (DeCarlo et al., 2006).  $PM_1$  mass in this study is taken as NR- $PM_1$  (from AMS) +  
104 black carbon (BC; measured by MAAP), which is appropriate for winter Seoul where refractory  $PM_1$  (metal/sea-  
105 salt/crustal) is minor and dust events were excluded (e.g., Kim et al., 2017; Nault et al., 2018; Kang et al., 2022;  
106 Jeon et al., 2023). Data were acquired at 2.5-minute intervals, alternating between V and W modes. The V mode  
107 provides higher sensitivity but lower resolution, suitable for mass quantification, whereas the W mode offers higher  
108 mass resolution but lower sensitivity, used here for OA source apportionment. Simultaneously, black carbon (BC)  
109 concentrations were measured at 1-minute intervals using a multi-angle absorption photometer (MAAP; Thermo  
110 Fisher Scientific, Waltham, MA, USA). Total  $PM_1$  mass was calculated as the sum of NR- $PM_1$  and BC.

111 Hourly trace gas concentrations (CO, O<sub>3</sub>, NO<sub>2</sub>, SO<sub>2</sub>) were obtained from the Gireum air quality monitoring station  
112 ( $37.61^{\circ}$  N,  $127.03^{\circ}$  E), managed by the Seoul Research Institute of Public Health and Environment. Meteorological

113 data (temperature, RH, wind speed/direction) were collected from the nearby Jungreung site (37.61° N, 127.00° E).  
114 All data are reported in Korea Standard Time (UTC+9).

115 To examine aerosol volatility, a thermodenuder (TD; Envalytix LLC) was installed upstream of the HR-ToF-AMS.  
116 Details are provided in Supplementary Section S1 Kang et al. (2022). Briefly, ambient flow alternated every 5  
117 minutes between a TD line and a bypass line at  $1.1 \text{ L min}^{-1}$ . Residence time in the TD line was  $\sim 6.3 \text{ s}$ . The TD  
118 setup included a 50 cm heating section followed by an adsorption unit. Heated particles were stripped of volatile  
119 species, while the downstream carbon-packed section prevented recondensation. TD temperature cycled through  
120 12 steps (30 to 200 °C), with each step lasting 10 min (total cycle = 120 min). AMS V and W modes were alternated  
121 during the same cycle. The heater was pre-adjusted to the next temperature while the bypass was active.

122

## 123 **2.3 Data Analysis**

124

### 125 **2.3.1 Data analysis and OA Source Apportionment**

126 HR-AMS data were processed using SQUIRREL v1.65B and PIKA v1.25B. Mass concentrations of non-refractory  
127 PM<sub>1</sub> (NR-PM<sub>1</sub>) species were derived from V-mode data, while high-resolution mass spectra (HRMS) and the  
128 elemental composition of organic aerosols (OA) were obtained from W-mode data. NR-PM<sub>1</sub> quantification  
129 followed established AMS protocols (Ulbrich et al., 2009; Zhang et al., 2011). Both the bypass and TD streams  
130 were processed using a time-resolved, composition-dependent collection efficiency CE(t) following Middlebrook  
131 et al. (2012). TD heating can modify particle water and phase state/mixing and thereby influence CE beyond  
132 composition (Huffman et al., 2009), but prior TD-AMS studies indicate that such effects are modest and largely  
133 multiplicative, which do not distort thermogram shapes or T<sub>50</sub> ordering (Faulhaber et al., 2009; Cappa & Jimenez,  
134 2010). In our data, the CE(t) statistics for the two lines were similar (campaign-average CE: TD =  $0.55 \pm 0.08$ ;  
135 bypass =  $0.53 \pm 0.04$ ;  $\Delta = 0.02 \approx 3.7\%$ , below the combined uncertainty  $\approx 0.09$ ). We therefore report volatility  
136 metrics with these line-specific CE(t) corrections applied and interpret potential residual CE effects as minor. For  
137 organics, elemental ratios (O:C, H:C, and OM/OC) were calculated using the Improved-Ambient (IA) method  
138 (Canagaratna et al., 2015). Positive Matrix Factorization (PMF) was applied to the HRMS of organics using the  
139 PMF2 algorithm (v4.2, robust mode) (Paatero and Tapper, 1994). The HRMS and corresponding error matrices  
140 from PIKA were analyzed using the PMF Evaluation Tool v2.05 (Ulbrich et al., 2009). Data pretreatment followed  
141 established protocols (Ulbrich et al., 2009; Zhang et al., 2011). A six-factor solution (fPeak = 0; Q/Q<sub>expected</sub> =  
142 3.56) was selected as optimal (Fig. S1). The resolved OA sources included hydrocarbon-like OA (HOA; 14%; O:C

143 = 0.13), cooking-related OA (COA; 21%; O:C = 0.18), nitrogen-enriched OA (NOA; 2%; O:C = 0.22), biomass-  
144 burning OA (BBOA; 13%; O:C = 0.25), less-oxidized oxygenated OA (LO-OOA; 30%; O:C = 0.68), and more-  
145 oxidized oxygenated OA (MO-OOA; 20%; O:C = 1.15) (Figs. S2 and S3). Alternative five- and seven-factor  
146 solutions were also evaluated. In the five-factor solution, the biomass burning source was not clearly resolved and  
147 appeared to be distributed across multiple factors. In the seven-factor solution, BBOA was further split into two  
148 separate factors without clear distinction or added interpretive value, making the six-factor solution the most  
149 physically meaningful and interpretable (Figs. S4 and S5). To ensure the statistical robustness of this solution, we  
150 calculated uncertainties for each PMF factor using the bootstrap method (100 iterations) with the PET toolkit (v2.05)  
151 (EPA, 2014; Xu et al., 2018; Srivastava et al., 2021) (Table S2 and Fig. S13).

152

### 153 **2.3.2 Thermogram and Volatility Estimation**

154 The chemical composition dependent mass fraction remaining (MFR) was derived at each TD temperature by  
155 dividing the corrected mass concentration of the TD line [p] by the average of the adjacent bypass lines [p-1] and  
156 [p+1]. Thermograms were corrected for particle loss, estimated using reference substances like NaCl, which exhibit  
157 minimal evaporation (Huffman et al., 2009; Saha et al., 2014; Kang et al., 2022). OA factor concentrations at each  
158 TD temperature were derived via multivariate linear regression between post-TD HRMS and ambient OA factor  
159 HRMS profiles as described in Zhou et al., 2017.

160 Volatility distributions were modeled using the thermodenuder mass transfer model from Riipinen et al. (2010) and  
161 Karnezi et al. (2014), implemented in Igor Pro 9 (Kang et al., 2022). OA mass was distributed into eight logarithmic  
162 saturation concentration bins ( $C^*$ : 1000 to  $0.0001 \mu\text{g m}^{-3}$ ). Modeled MFRs were fit to observations using Igor's  
163 "FuncFit" function, repeated 1,000 times per OA factor to determine best-fit results. The model assumes no thermal  
164 decomposition and includes adjustable parameters: mass accommodation coefficient ( $\alpha_m$ ) and enthalpy of  
165 vaporization ( $\Delta H_{\text{exp}}$ ), randomly sampled within literature-based ranges (Table S1).

166

## 167 **3 Results and discussion**

### 168 **3.1 Overview of PM<sub>1</sub> Composition and OA Sources**

169 We conducted continuous measurements from 28 November to 28 December 2019, characterizing a winter period  
170 with a mean PM<sub>1</sub> concentration of  $27.8 \pm 15.3 \mu\text{g m}^{-3}$ . This concentration is characterized as moderate; it closely  
171 matches historical winter PM<sub>1</sub> means in Seoul (Kim et al., 2017) and implies an equivalent PM<sub>2.5</sub> concentration is

172 about  $34.8 \mu\text{gm}^{-3}$  (using a Korea-specific  $\text{PM}_1/\text{PM}_{2.5} \approx 0.8$  (Kwon et al., 2023), which is near the national 24-h  $\text{PM}_{2.5}$   
173 standard ( $35 \mu\text{gm}^{-3}$ ) (AirKorea). The full co-evolution of  $\text{PM}_1$ , gaseous pollutants, and meteorological conditions  
174 is provided in Fig. S6, showing an average ambient temperature of  $1.76 \pm 4.3^\circ\text{C}$  and average relative humidity (RH)  
175 of  $56.9 \pm 17.5\%$  during the study.

176 Figure 1 summarizes the overall non-refractory submicron aerosol (NR- $\text{PM}_1$ ) composition and the identified OA  
177 factors. Organics (41%) and nitrate (30%) were the most abundant chemical components of  $\text{PM}_1$ , followed by  
178 ammonium (12%), sulfate (10%), BC (5%), and chloride (3%) (Fig. 1a). Among the organic aerosols, six OA  
179 factors were identified during the winter of 2019: hydrocarbon-like OA (HOA; 14%; O:C = 0.13), cooking-related  
180 OA (COA; 21%; O:C = 0.18), nitrogen-enriched OA (NOA; 2%; O:C = 0.22), biomass burning OA (BBOA; 13%;  
181 O:C = 0.25), and two types of secondary organic aerosols—less-oxidized oxygenated OA (LO-OOA; 30%; O:C =  
182 0.68) and more-oxidized oxygenated OA (MO-OOA; 20%; O:C = 1.15) (Fig. 1e and Fig. S2). These compositions  
183 are consistent with previous wintertime observations in Kim et al. (2017), with the exception of newly resolved  
184 NOA source. In the following sections, we describe each OA factor in the order of secondary OA (SOA), primary  
185 OA (POA) and finally introduce NOA, which—while related to combustion POA—emerged as a distinct, nitrogen-  
186 rich factor under the winter conditions of this study.

187  $\text{PM}_1$  mass concentrations varied widely, ranging from  $4.61$  to  $91.4 \mu\text{g m}^{-3}$ , largely due to two severe haze episodes  
188 that occurred between December 7–12 and December 22–26 (Fig. 1). During these episodes, average  
189 concentrations increased significantly, driven primarily by elevated levels of nitrate and organic aerosols—  
190 particularly MO-OOA and NOA (Fig. 1f,g). Back-trajectory clustering shows frequent short-range recirculation  
191 over the Seoul Metropolitan Area during haze (Cluster 1; Fig. S8), and the time series indicates persistently low  
192 surface wind speeds during these periods ( $1.73 \pm 0.89$  vs.  $2.34 \pm 1.18$  (clean)) (Fig. S6). These patterns indicate  
193 stagnation-driven accumulation of local emissions, consistent with the simultaneous increase of MO-OOA and  
194 NOA that are examined in detail in subsequent sections. Such haze episodes, characterized by local emission  
195 buildup and secondary aerosol production, are a typical wintertime feature, as also reported in Kim et al. (2017).

### 196 3.1.1 Secondary organic aerosols (SOA)

197 In this study, two OOA factors—more-oxidized OOA (MO-OOA) and less-oxidized OOA (LO-OOA)—were  
198 identified, together accounting for approximately half of the total organic aerosol (OA) mass. This fraction is  
199 notably higher than that reported in previous wintertime urban studies (Kim et al., 2017; Zhang et al., 2007). Both

200 OOAs exhibited characteristic mass spectral features, including prominent peaks at  $m/z$  44 ( $\text{CO}_2^+$ ) and  $m/z$  43  
201 ( $\text{C}_2\text{H}_3\text{O}^+$ ), which are widely recognized as markers of oxygenated organics (Fig. S2e, S3f). The oxygen-to-carbon  
202 (O:C) ratios for MO-OOA and LO-OOA were 1.15 and 0.68, respectively, indicating both factors are highly  
203 oxidized relative to the primary OA factors (HOA, COA, BBOA) and that MO-OOA is substantially more oxidized  
204 than LO-OOA. The O:C ratio of MO-OOA was especially elevated, exceeding those reported in previous Seoul  
205 campaigns—0.68 in winter 2015 (Kim et al., 2017), 0.99 in spring 2019 (Kim et al., 2020), and 0.78 in fall 2019  
206 (Jeon et al., 2023)—while the LO-OOA ratio was within a similar range.

207 MO-OOA showed strong correlations with secondary inorganic species such as nitrate ( $r = 0.90$ ), ammonium ( $r =$   
208 0.92), and sulfate ( $r = 0.81$ ), consistent with its formation through regional and local photochemical aging processes  
209 (Fig. S3). In contrast, LO-OOA exhibited only modest correlations with sulfate, nitrate, and ammonium ( $r = 0.50$ ,  
210 0.51, and 0.42, respectively). This weaker coupling indicates that LO-OOA represents a less aged oxygenated OA  
211 component (fresh SOA), distinguishable from the more aged, highly processed MO-OOA which tracks closely with  
212 secondary inorganic species. Regarding potential primary influence, LO-OOA does not exhibit a pronounced  $m/z$   
213 60 (levoglucosan) signal (Figs. S2 and 9). While the levoglucosan marker ( $f_{60}$ ) is known to diminish with  
214 atmospheric aging and can become weak or undetectable downwind (Hennigan et al., 2010; Cubison et al., 2011),  
215 the absence of a distinct peak combined with the separation from inorganic salts suggests that LO-OOA is best  
216 characterized as freshly formed secondary organic aerosol likely originating from the rapid oxidation of local  
217 anthropogenic precursors.

### 218 3.1.2 Primary organic aerosols (POA)

219 Three primary organic aerosol (POA) factors were identified in this study: hydrocarbon-like OA (HOA), cooking-  
220 related OA (COA), and biomass burning OA (BBOA). These three components exhibited mass spectral and  
221 temporal characteristics consistent with previous observations in Seoul and other urban environments. HOA was  
222 characterized by dominant alkyl fragment ions ( $\text{C}_n\text{H}_{2n+1}^+$  and  $\text{C}_n\text{H}_{2n-1}^+$ ; Fig. S2a) and a low O:C ratio (0.13),  
223 consistent with traffic-related emissions (0.05–0.25) (Canagaratna et al., 2015). It showed strong correlations with  
224 vehicle-related ions  $\text{C}_3\text{H}_7^+$  ( $r = 0.79$ ) and  $\text{C}_4\text{H}_9^+$  ( $r = 0.86$ ) (Kim et al., 2017; Canagaratna et al., 2004; Zhang et al.,

225 2005), and exhibited a distinct morning rush hour peak (06:00–08:00), followed by a decrease likely driven by  
226 boundary layer expansion (Fig. S3a).

227 COA, accounting for 21% of OA, showed higher contributions from oxygenated ions than HOA, with tracer peaks  
228 at  $m/z$  55, 84 and 98 (Fig. S2b) consistent with cooking emissions (Sun et al., 2011). COA showed an enhanced  
229 signal at  $m/z$  55 relative to  $m/z$  57, with a 55/57 ratio of 3.11, substantially larger than that of HOA (1.10). This  
230 elevated ratio is consistent with previously reported AMS COA spectra in urban environments (e.g., Allan et al.,  
231 2010; Mohr et al., 2012; Sun et al., 2011), supporting our factor assignment. It correlated strongly with cooking-  
232 related ions such as  $\text{C}_3\text{H}_3\text{O}^+$  ( $r = 0.94$ ),  $\text{C}_5\text{H}_8\text{O}^+$  ( $r = 0.96$ ), and  $\text{C}_6\text{H}_{10}\text{O}^+$  ( $r = 0.98$ ) (Fig. S3h), and displayed  
233 prominent peaks during lunch and dinner hours, reflecting typical cooking activity patterns.

234 BBOA was identified based on characteristic ions at  $m/z$  60 ( $\text{C}_2\text{H}_4\text{O}_2^+$ ) and 73 ( $\text{C}_3\text{H}_5\text{O}^+$ ), both of which are  
235 associated with levoglucosan—a well-established tracer for biomass burning (Simoneit et al., 2002). Its relatively  
236 high  $f_{60}$  and low  $f_{44}$  values (Fig. S9) indicate that the BBOA observed in this study was relatively fresh and had not  
237 undergone extensive atmospheric aging (Cubison et al., 2011). Regarding source location, several pathways can  
238 influence Seoul’s biomass burning signature. First, urban/peri-urban small-scale burning (e.g., solid-fuel use in  
239 select households, restaurant charcoal use, and intermittent waste burning) has been reported and can enhance  
240 BBOA locally (Kim et al., 2017). Second, nearby agricultural-residue burning in surrounding provinces occurs  
241 seasonally and can episodically impact the metropolitan area (Han et al., 2022). Third, regional transport from  
242 upwind regions (e.g., northeastern China/North Korea) can bring biomass burning influenced air masses under  
243 northerly/northwesterly flow (Lamb et al., 2018; Nault et al., 2018). In this dataset, the nighttime and early-  
244 morning enhancements and trajectory clusters showing regional recirculation indicate a predominantly local/near-  
245 source contribution during the study period, with episodic non-local influences remaining possible.

#### 246 3.1.3 Nitrogen-containing organic aerosol (NOA)

247 A distinct nitrogen-containing organic aerosol (NOA) factor was resolved in this study, whereas earlier wintertime  
248 AMS–PMF analyses in Seoul did not isolate such a component. The NOA factor exhibited the highest nitrogen-to-  
249 carbon (N:C) ratio (0.22) and the lowest oxygen-to-carbon (O:C) ratio (0.19) among all POA factors (Fig. S2),  
250 indicating a chemically reduced, nitrogen-rich composition. The NOA mass spectrum was dominated by amine-  
251 related fragments including  $m/z$  30 ( $\text{CH}_4\text{N}^+$ ), 44 ( $\text{C}_2\text{H}_6\text{N}^+$ ), 58 ( $\text{C}_3\text{H}_8\text{N}^+$ ), and 86 ( $\text{C}_5\text{H}_{12}\text{N}^+$ ) (Fig. 3a). The spectral  
252 signature of the factor is defined by the characteristic dominance of the  $m/z$  44 fragment, which typically serves as

253 the primary marker for dimethylamine (DMA)-related species, closely followed by  $m/z$  58 (trimethylamine, TMA)  
254 and  $m/z$  30 (methylamine, MA). This profile is in strong agreement with NOA factors resolved via PMF in other  
255 polluted environments. For instance, the dominance of  $m/z$  44 and  $m/z$  30 aligns with amine factors reported in  
256 New York City (Sun et al., 2011) and Pasadena, California (Hayes et al., 2013). This DMA-dominated signature is  
257 also consistent with seasonal characterization of organic nitrogen in Beijing (Xu et al., 2017) and Po Valley, Italy  
258 (Saarikoski et al., 2012), reinforcing the common chemical signature of reduced organic nitrogen across diverse  
259 urban and regional environments. Furthermore, the presence of non-negligible signals at  $m/z$  58 and  $m/z$  86 supports  
260 the contribution of slightly larger alkylamines, a pattern that aligns well with established AMS laboratory reference  
261 spectra for these reduced nitrogen compounds (Ge et al., 2011; Silva et al., 2008).

262 These amines are commonly emitted during the combustion of nitrogen-rich biomass and proteinaceous materials  
263 and are frequently associated with biomass-burning emissions (Ge et al., 2011). Previous molecular analyses in  
264 Seoul also indicate DMA, MA, and TMA as the dominant amine species in December (Baek et al., 2022). While  
265 other amines such as triethylamine (TEA), diethylamine (DEA), and ethylamine (EA) may contribute via  
266 industrial/solvent pathways (e.g., chemical manufacturing, petrochemical corridors, wastewater treatment), our  
267 HR-AMS spectra are dominated by small alkylamine fragments ( $m/z$  30, 44, 58, 86) and the diurnal behavior co-  
268 varies with combustion markers (Fig. 2), indicating a primarily combustion-linked influence. Nevertheless, recent  
269 urban measurements and sector-based analyses show that industrial activities can contribute measurable amines in  
270 cities (Tiszenkel et al., 2024; Zheng et al., 2015; Mao et al., 2018; Shen et al., 2017; Yao et al., 2016). Accordingly,  
271 a minor NOA contribution from solvent/industrial amines cannot be excluded. NOA exhibited a nighttime–early-  
272 morning enhancement (Fig. 2a), similar to BBOA, indicating that both factors are influenced by wintertime  
273 combustion and residential heating, which are known sources of small alkylamines and amides (You et al., 2014;  
274 Yao et al., 2016). Strong correlations of NOA with  $\text{CH}_4\text{N}^+$  ( $r = 0.95$ ) and  $\text{C}_2\text{H}_6\text{N}^+$  ( $r = 0.91$ ) (Fig. 2) further support  
275 the presence of reduced-nitrogen species associated with these combustion activities. However, the time series of  
276 NOA and BBOA are not strongly correlated (Fig. 2 and Fig. S7). This contrast reflects their differing behaviors:  
277 BBOA follows a relatively regular daily emission pattern, whereas NOA appears predominantly during stagnant  
278 haze periods (Fig. 1) when cold, humid, and low-wind conditions allow semi-volatile amines to partition to the  
279 particle phase and form low-volatility aminium salts. Thus, NOA in wintertime Seoul likely reflects a combination

280 of shared primary combustion influences and enhanced secondary processing of amine-containing precursors under  
281 meteorological conditions that favor partitioning and accumulation.

282 Detection of particulate NOA using real time measurement has been challenging due to its low concentration and  
283 high volatility. Although Baek et al. (2022) identified nitrogen-containing species in Seoul via year-round filter-  
284 based molecular analysis, PMF-based resolution of NOA in real time has not been previously reported. The  
285 successful identification in this study is likely attributable to favorable winter meteorological conditions—  
286 specifically low temperatures ( $-0.24^{\circ}\text{C}$ ) and persistently high relative humidity ( $\sim 57\%$ ) compared to the 2017  
287 winter season (Kim et al., 2017)—that enhanced gas-to-particle partitioning of semi-volatile amines, thereby  
288 enabling their detection (Fig. S2). NOA concentrations frequently exceeded  $1 \mu\text{g m}^{-3}$  when RH surpassed 60% (Fig.  
289 2), supporting the importance of RH-driven partitioning and the subsequent formation of low-volatility aminium  
290 salts (Rovelli et al., 2017). Although extremely low temperatures may inhibit NOA formation due to the transition  
291 of aerosol particles into solid phase (Ge et al., 2011; Srivastava et al., 2022), the combination of consistently cold  
292 and humid conditions during the measurement period likely promoted the partitioning of semi-volatile amines into  
293 the particle phase. In addition, episodic haze events further elevated NOA levels, increasing its contribution to OA  
294 from 1% during clean periods to as much as 3% (Fig. 1f–h). These high-concentration events likely improved the  
295 signal-to-noise ratio, facilitating PMF resolution. Back-trajectory clustering indicates that NOA-enhanced events  
296 were dominated by short-range recirculation (Cluster 1; Fig. S7), consistent with the short atmospheric lifetimes  
297 and high reactivity of alkylamines (Nielsen et al., 2012; Hanson et al., 2014). Overall, the factor reflects semi-  
298 volatile, reduced-nitrogen species originating from primary urban combustion sources, with their observed particle-  
299 phase mass amplified by rapid secondary partitioning and salt formation under seasonally favorable conditions.

300

301 NOA contributed approximately 2 % of total OA, comparable to urban contributions reported in Guangzhou (3 %;  
302 Chen et al., 2021), Pasadena (5 %; Hayes et al., 2013), and New York (5.8 %; Sun et al., 2011). These similarities  
303 suggest that the NOA factor observed in Seoul reflects a broader class of urban wintertime reduced-nitrogen  
304 aerosols rather than a site-specific anomaly. In most urban environments, the detectability of NOA appears to  
305 depend strongly on the interplay between emission strength, stagnation, and humidity—which together govern the  
306 particle-phase partitioning of volatile amines.

307 **3.2 Volatility of Non-Refractory Species**

308 Figure 4 presents thermograms of non-refractory (NR) species measured by HR-ToF-AMS. The mass fraction  
309 remaining (MFR) after thermodenuder (TD) treatment follows the typical volatility trend reported in previous  
310 studies (Xu et al., 2016; Kang et al., 2022; Jeon et al., 2023; Huffman et al., 2009): nitrate was the most volatile,  
311 followed by chloride, ammonium, organics, and sulfate. Nitrate showed the steepest decline with increasing  
312 temperature, with a  $T_{50}$  of  $\sim 67$  °C—substantially higher than that of pure ammonium nitrate ( $\sim 37$  °C; Huffman et  
313 al., 2009). At 200 °C,  $\sim 2\%$  of the initial nitrate signal remained (Fig. 4). Since pure ammonium nitrate fully  
314 evaporates well below this temperature (Huffman et al., 2009), this small residual fraction likely represents the  
315 least volatile portion of organic nitrates. Compared to previously reported fall conditions ( $T_{50} \sim 73$  °C, incomplete  
316 evaporation), winter nitrate appeared more volatile, indicating relatively fewer non-volatile nitrate forms (e.g.,  
317 Kang et al., 2022; Jeon et al., 2023). Sulfate exhibited the highest thermal stability among the measured species.  
318 The thermogram showed a relatively stable mass fraction (MFR  $> 0.8$ ) up to  $\sim 130$  °C, followed by a sharp decline  
319 at temperatures above 140 °C (Fig. 4). This profile is consistent with the typical volatilization behavior of  
320 ammonium sulfate in TD-AMS, which requires higher temperatures to evaporate compared to nitrate or organics  
321 (Huffman et al., 2009). At 200 °C, approximately 25% of the sulfate mass remained. This residual suggests the  
322 presence of a sulfate fraction with lower volatility than pure ammonium sulfate, likely associated with  
323 organosulfates or low-volatility mixtures, whereas refractory metal sulfates are not efficiently detected by the AMS  
324 (Canagaratna et al., 2007). Ammonium showed intermediate volatility, with  $T_{50}$  between nitrate and sulfate. Its  
325 slightly lower winter  $T_{50}$  suggests stronger nitrate association. Residual ammonium at 200 °C was consistent ( $\sim 4\%$ )  
326 in previously reported spring/fall measurements (Kang et al., 2022; Jeon et al., 2023). Chloride volatility was  
327 broadly consistent with prior AMS studies, with  $T_{50}$  values comparable across seasons (e.g., Xu et al., 2016; Jeon  
328 et al., 2023). The near-complete evaporation observed in winter ( $\sim 4\%$  residual at 200 °C, Fig. 4) indicates that the  
329 chloride measured here was dominated by volatile inorganic chloride, specifically ammonium chloride ( $\text{NH}_4\text{Cl}$ ),  
330 which fully evaporates at relatively low temperatures (Huffman et al., 2009). By contrast, metal chlorides (e.g.,  
331  $\text{NaCl}$ ,  $\text{KCl}$ ) are refractory and far less volatile; they are also poorly detected by the AMS (Canagaratna et al., 2007).  
332 The lower residual in winter compared to fall ( $\sim 10\%$ ) therefore suggests that wintertime chloride consisted almost  
333 exclusively of pure ammonium chloride, whereas the fall samples may have contained a minor fraction of less  
334 volatile or refractory chloride species. Organics exhibited moderate volatility ( $T_{50} \sim 120$  °C), and their thermogram  
335 showed a gradual, continuous decrease in mass fraction with increasing TD temperature. This smooth profile  
336 reflects the presence of a broad distribution of organic compounds spanning SVOC to LVOC ranges, in contrast to

337 inorganic species such as nitrate or ammonium chloride, which often show more abrupt losses at characteristic  
338 temperatures (Huffman et al., 2009; Xu et al., 2016). This behavior is consistent with previous TD-AMS  
339 observations in Seoul during spring and fall (Kang et al., 2022; Jeon et al., 2023).

340 **3.2.1 Volatility Profiles of Organic sources**

341 Figure 5 presents the volatility distributions of six OA sources within the volatility basis set (VBS) framework.  
342 Volatility is expressed as the effective saturation concentration ( $C^*$ ,  $\mu\text{g m}^{-3}$ ), where higher  $C^*$  values correspond  
343 to higher volatility. Following Donahue et al. (2009),  $C^*$  values are categorized into four bins: extremely low-  
344 volatility organic compounds (ELVOCs,  $\log C^* < -4.5$ ), low-volatility organic compounds (LVOCs,  $-4.5 < \log$   
345  $C^* < -0.5$ ), semi-volatile organic compounds (SVOCs,  $-0.5 < \log C^* < 2.5$ ), and intermediate-volatility organic  
346 compounds (IVOCs,  $2.5 < \log C^* < 6.5$ ).

347 Among the primary OA (POA) sources, hydrocarbon-like OA (HOA) exhibited the highest volatility, with mass  
348 predominantly distributed in the SVOC and IVOC ranges, consistent with its chemically reduced nature ( $\text{O:C} =$   
349 0.13) and direct combustion origin. Mass fraction remaining (MFR) results (Fig. S9) further support this, showing  
350 rapid mass loss at lower temperatures. Biomass burning OA (BBOA) and nitrogen-containing OA (NOA) also  
351 showed high volatility, peaking in the SVOC–IVOC range ( $\log C^* = 1–3$ ), but displayed slightly higher O:C ratios  
352 (0.25 and 0.19, respectively). This modest enhancement in O:C reflects their source composition—biomass  
353 combustion produces partially oxygenated organic species (e.g., levoglucosan, phenols), and NOA contains  
354 nitrogen-bearing functional groups—rather than enhanced atmospheric oxidation. Cooking-related OA (COA)  
355 showed a more moderate volatility profile, with mass more evenly distributed across the LVOC and SVOC bins.  
356 This behavior differs from that of BBOA, which is slightly more oxidized yet more volatile. This apparent  
357 decoupling between oxidation state and volatility is a characteristic feature of COA reported in previous volatility  
358 studies (Paciga et al., 2016; Kang et al., 2022). These studies attribute the lower volatility of COA to its abundance  
359 of high-molecular-weight fatty acids (e.g., oleic, palmitic, and stearic acids) and glycerides (Mohr et al., 2009; He  
360 et al., 2010). Unlike the smaller, fragmented molecules typical of biomass burning, these lipid-like compounds  
361 possess high molar masses that suppress volatility, even though their long alkyl chains result in low O:C ratios.

362 For secondary OA (SOA), less-oxidized oxygenated OA (LO-OOA) exhibited the lowest volatility, with substantial  
363 mass in the LVOC and ELVOC bins ( $C^* \approx 10^{-3}–10^{-4}$ ). This is in agreement with previous findings in Seoul during  
364 spring (Kang et al., 2022). In contrast, more-oxidized OOA (MO-OOA), despite its higher oxidation state ( $\text{O:C} =$

365 1.15), displayed greater volatility, with a peak at  $C^* \approx 10^1$ . This discrepancy likely reflects differences in formation  
366 and aging processes, as discussed further in Section 3.3.

367 Overall, the volatility characteristics across OA factors suggest that oxidation state alone does not fully explain  
368 volatility. Rather, volatility is shaped by a combination of emission source, emission timing, temperature, and  
369 atmospheric processing. These findings highlight the importance of integrating both chemical and physical  
370 characterization to better understand OA formation and aging across seasons.

### 371 **3.3 Aging effect on volatility from 2D VBS**

372 Generally, the oxygen-to-carbon (O:C) ratio of organic aerosols (OA) is inversely related to their volatility. As O:C  
373 increases through aging, the effective saturation concentration ( $C^*$ ) typically decreases, resulting in lower volatility  
374 (Donahue et al., 2006; Jimenez et al., 2009). This relationship arises because oxidative functionalization introduces  
375 polar groups (e.g., hydroxyl, carboxyl) that increase molecular weight and enhance intermolecular hydrogen  
376 bonding, thereby reducing the effective saturation concentration ( $C^*$ ) and promoting particle-phase retention  
377 (Jimenez et al., 2009; Kroll and Seinfeld, 2008; Donahue et al., 2011). However, in this study, the most oxidized  
378 OA factor—MO-OOA, with a high O:C ratio of 1.15—exhibited unexpectedly high volatility. Its volatility  
379 distribution was skewed toward SVOCs and IVOCs (Fig. 5), and its rapid mass loss in MFR thermograms (Fig. S9)  
380 further indicated low thermal stability. This observation appears to contradict the usual inverse O:C–volatility  
381 relationship; however, under winter haze conditions—with suppressed  $O_3$ /low OH, particle-phase autoxidation and  
382 fragmentation can yield higher-O:C yet more volatile products, with enhanced condensation on abundant particle  
383 surface area (details below).

384 Viewed against prior TD-AMS results, the volatility of Seoul’s winter MO-OOA presents a unique case,  
385 particularly in the nature of its O:C-volatility relationship. Prior urban studies have commonly reported substantial  
386 SVOC-OA, consistent with high photochemical activity or elevated loadings; for example, prior TD-AMS studies  
387 in Mexico City, Los Angeles, Beijing, and Shenzhen have all reported substantial SVOC–IVOC contributions  
388 during polluted periods, indicating that high OA volatility is a common feature of urban environments across  
389 seasons (Cappa and Jimenez, 2010; Xu et al., 2019; Cao et al., 2018). While these comparisons establish that  
390 volatile OA is common, they generally did not report the factor-level inversion observed here, where the highly-  
391 oxidized OOA component (MO-OOA) was more volatile than a less-oxidized OOA (LO-OOA). This behavior is  
392 distinct from findings in colder, lower-loading regimes; wintertime Paris, for instance, maintained the conventional

393 hierarchy where the more-oxidized OOA was comparatively less volatile (Paciga et al., 2016). Furthermore,  
394 seasonal context within Seoul showed springtime OA with lower oxidation levels than our winter MO-OOA despite  
395 similar SVOC contributions (Kang et al., 2022). This comprehensive comparison underscores the unusual nature  
396 of the O:C-volatility relationship observed under the specific winter haze conditions in Seoul.

397

### 398 **3.3.1 High-volatility nature of MO-OOA in Seoul wintertime**

399 MO-OOA exhibited high O:C ratios and high apparent volatility, characteristics that were further amplified during  
400 haze episodes—periods marked by reduced ozone levels, low solar radiation, and elevated aerosol mass  
401 concentrations (Fig. 7 and Fig. S6, yellow shading). Spectrally, MO-OOA was defined by a consistently high  $f_{44}$   
402 ( $\text{CO}_2^+$ ) signal and a comparatively stable  $f_{43}$  ( $\text{C}_2\text{H}_3\text{O}^+$ ) signal relative to LO-OOA (Fig. 6). Notably, when MO-  
403 OOA concentrations intensified during haze, only  $f_{44}$  was significantly enhanced, while  $f_{43}$  remained nearly  
404 unchanged (Fig. 6). This trend is corroborated by the haze–non-haze comparison (Fig. S12), where haze periods  
405 (including high MO-OOA intervals) showed elevated contributions from oxygenated fragments ( $m/z$  28, 29, 44)  
406 and higher O:C ratios. In contrast, non-haze periods were characterized by larger fractional contributions from  
407 hydrocarbon-like fragments ( $m/z$  41, 43, 55, 57). The observed temporal pattern—elevated  $f_{44}$  without  
408 corresponding changes in  $f_{43}$ —is a typical signature of highly oxidized and fragmented organic aerosol (Figs. 6 and  
409 7), suggesting that aging was dominated by fragmentation rather than functionalization (Kroll et al., 2009). These  
410 spectral patterns collectively indicate that MO-OOA is highly oxidized yet remains relatively volatile compared to  
411 LO-OOA.

412 The elevated volatility of MO-OOA despite its high O:C (~1.15) indicates that oxidation under these haze  
413 conditions did not follow the classical multi-generational OH-driven aging pathway, which typically increases  
414 molecular mass and reduces volatility. Instead, the data align with fragmentation-dominated aging, where highly  
415 oxygenated but lower-molecular-weight compounds (e.g., small acids or diacids) are formed. Prior field and  
416 laboratory studies using online AMS/FIGAERO-CIMS and EESI-TOF have similarly reported high-O:C yet  
417 volatile product distributions characterized by high  $f_{44}$  and stable  $f_{43}$  (Kroll et al., 2009; Ng et al., 2010; Chhabra et  
418 al., 2011; Lambe et al., 2012; Lopez-Hilfiker et al., 2016; D’Ambro et al., 2017).

419 While direct mechanistic measurements were not available in this study, we hypothesize that the formation of this  
420 volatile, high-O:C component may be driven by specific low-light oxidation pathways consistent with the observed  
421 environmental conditions. The suppressed ozone levels during haze likely indicate a low-OH oxidation regime (Fig.

422 7). Under such conditions, radical chemistry involving  $\text{NO}_3$  (which is longer-lived in low light) or particle-phase  
423 autoxidation could preferentially produce highly oxygenated but relatively small organic fragments (Ehn et al.,  
424 2014; Zhao et al., 2023). Although haze suppresses photolysis,  $\text{HONO}$  concentrations—maintained via  
425 heterogeneous conversion or surface emissions—could still provide a non-negligible source of  $\text{OH}$  (Gil et al., 2021;  
426 Kim et al., 2024; Slater et al., 2020). Furthermore, the high aerosol mass loadings during haze ( $C_{\text{oa}}$ ) provide  
427 abundant surface area for absorptive partitioning (Pankow, 1994; Donahue et al., 2006). This increased partitioning  
428 mass allows even relatively volatile, oxidized compounds to condense into the particle phase, contributing to the  
429 high apparent volatility and oxidation state observed (Jimenez et al., 2009; Ng et al., 2016). Consequently, these  
430 results underscore the need for SOA models to incorporate fragmentation-dominated pathways to accurately  
431 represent wintertime haze evolution.

## 432 4 Conclusions

433 This study provides a comprehensive characterization of wintertime submicron aerosols ( $\text{PM}_1$ ) in Seoul, integrating  
434 chemical composition, volatility measurements, and source apportionment to reveal critical insights into urban OA  
435 evolution. The two most significant findings are the robust real-time identification of a nitrogen-containing organic  
436 aerosol (NOA) factor and the observation of unexpected volatility behavior in highly oxidized OA. The NOA factor,  
437 spectrally dominated by low-molecular-weight alkylamine fragments, was successfully resolved primarily due to  
438 the accumulation of pollutants during wintertime stagnation, which sufficiently enhanced the spectral signals of  
439 these semi-volatile species for identification. Its temporal and chemical characteristics point to a mixed  
440 primary/secondary origin: driven by direct combustion emissions (e.g., residential heating) but significantly  
441 enhanced by the rapid gas-to-particle partitioning of semi-volatile amines under cold, humid conditions.  
442 Concurrently, the volatility analysis revealed a striking decoupling between oxidation state and volatility for the  
443 More-Oxidized Oxygenated OA (MO-OOA). Despite its high O:C ratio (~1.15), MO-OOA exhibited elevated  
444 volatility, a deviation from classical aging models that typically associate high oxidation with low volatility. This  
445 behavior is attributed to the specific conditions of winter haze—reduced photolysis and high aerosol mass  
446 loadings—which favor fragmentation-dominated aging pathways and the absorptive partitioning of volatile  
447 oxygenated products.

448 These results revise our understanding of wintertime aerosol dynamics and underscore the limitations of current  
449 models in representing reduced-nitrogen species and non-canonical oxidation pathways. To address the remaining

450 uncertainties, future research should prioritize evaluating the seasonal variability of NOA to better disentangle the  
451 influence of meteorological drivers from specific emission sources. Concurrently, there is a critical need to directly  
452 probe radical oxidation mechanisms, such as  $\text{RO}_2$  autoxidation and  $\text{NO}_3$  chemistry, particularly under haze  
453 conditions. Integrating these field inquiries with laboratory studies and advanced molecular-level measurements  
454 (e.g., FIGAERO-CIMS, EESI-TOF) will be essential for constraining the formation, lifetime, and climate impacts  
455 of these complex organic aerosol components in polluted megacities.

456 **Data availability.**

457 Data presented in this article are available upon request to the corresponding author.

458 **Acknowledgements**

459 This work was supported by the National Research Foundation of Korea (NRF) grant funded by the Korea government (MSIT)  
460 (RS-2025-00514570), the project “development of SMaRT based aerosol measurement and analysis systems for the evaluation  
461 of climate change and health risk assessment” operated by Seoul National University (900-20240101).

462 **Author Contributions**

463 Hwajin Kim designed and prepared the manuscript. Jiwoo Jeong operated the TD-AMS and analyse the data. Jihye Moon  
464 analyse the data. Hyungu Kang analyse the volatility of OA.

465

466 **Competing interests.**

467 The authors declare that they have no conflict of interest.

468

469

470

471

472

473

474

475

476

477

478

479

480

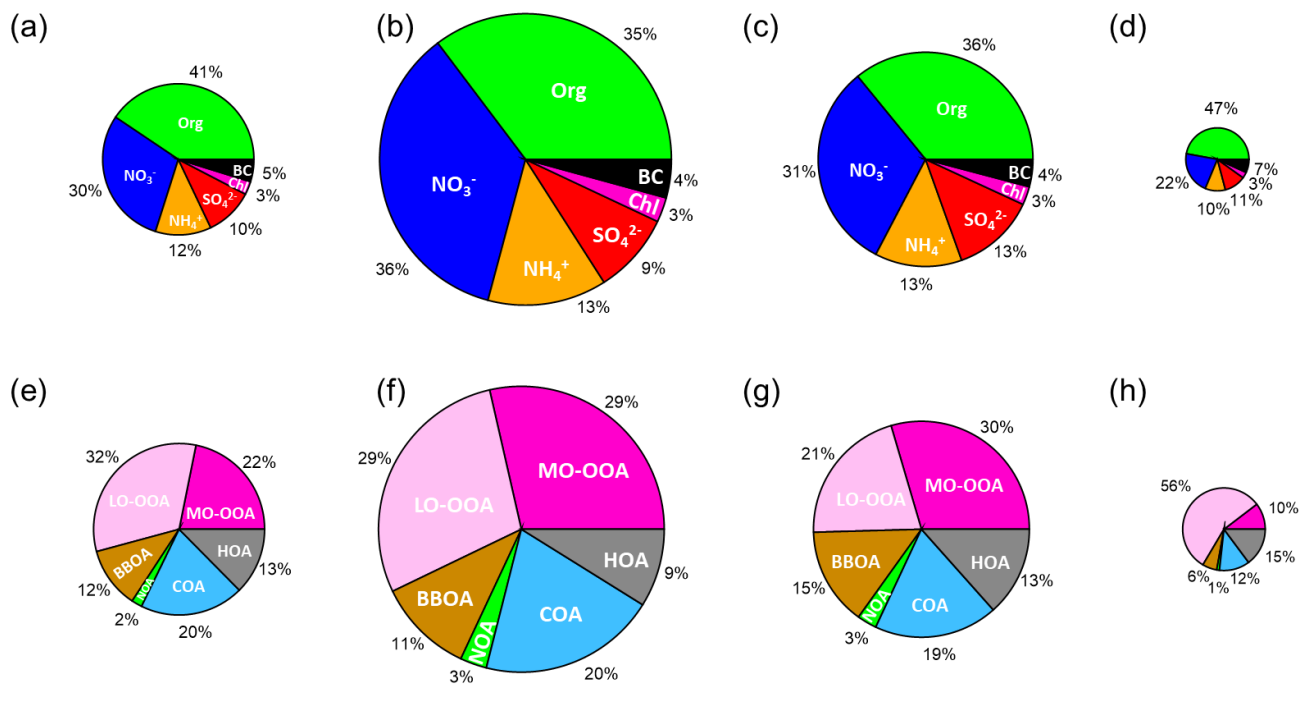
481

482

483

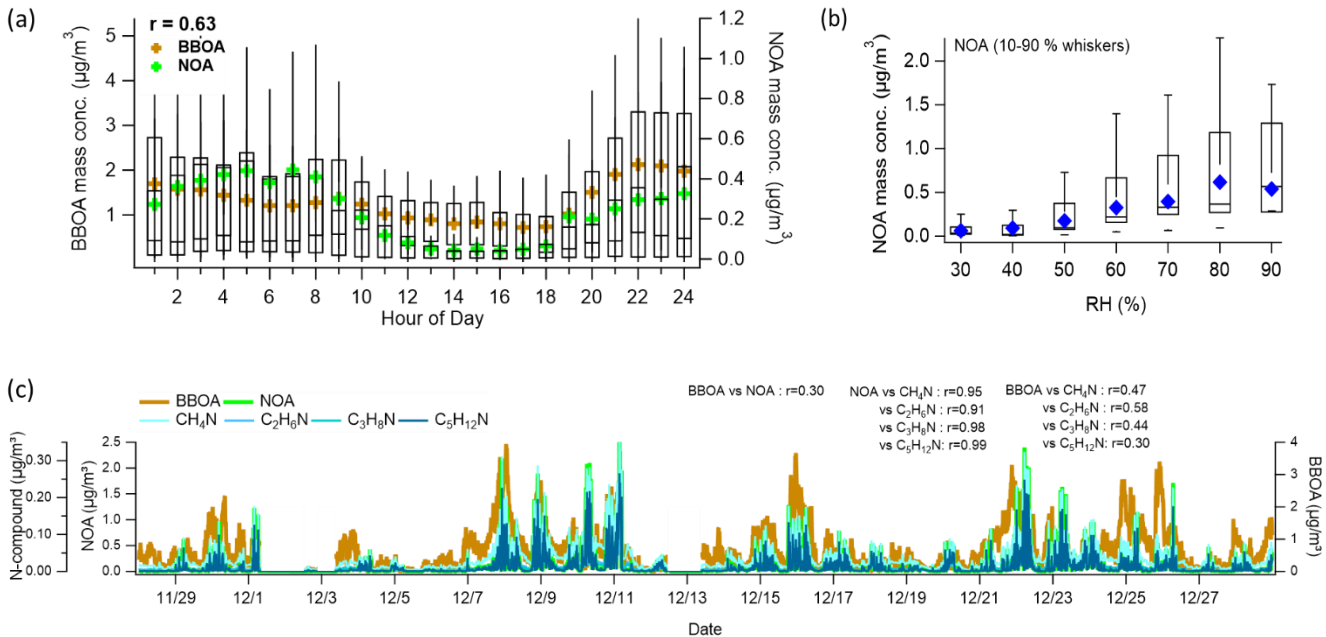
484

485



	Period	Standard	Avg. Mass conc. ( $\mu\text{g m}^{-3}$ )
<b>Total</b>	2019.11.28 ~ 2019.12.28		Avg $\text{PM}_1 = 26.37$
<b>Clean</b>	2019.12.04 ~ 2019.12.06	Daily $\text{PM}_1 < 10.00 \mu\text{g m}^{-3}$	Avg $\text{PM}_1 = 9.98$
<b>Haze 1</b>	2019.12.07 ~ 2019.12.11	Daily $\text{PM}_1 > 30.00 \mu\text{g m}^{-3}$	Avg $\text{PM}_1 = 51.88$
<b>Haze 2</b>	2019.12.21 ~ 2019.12.25	Daily $\text{PM}_1 > 30.00 \mu\text{g m}^{-3}$	Avg $\text{PM}_1 = 37.71$

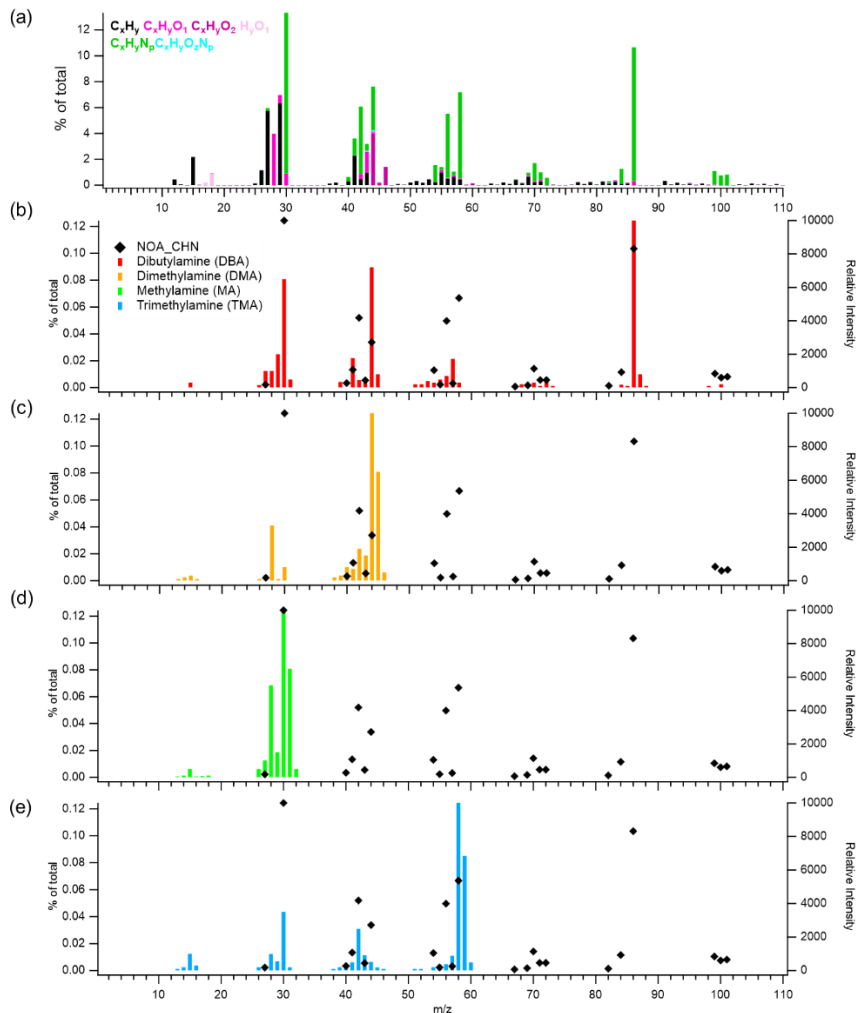
492 **Figure 1.** Compositional pie charts of  $\text{PM}_1$  species for (a) the entire study period, (b) haze period 1, (c) haze period 2, and  
 493 (d) a clean period; and of each OA source for (e) the entire study period, (f) haze period 1, (g) haze period 2, and (h) the  
 494 clean period. Table. Standard and average  $\text{PM}_1$  mass concentrations during the entire study period, haze period 1, haze period  
 495 2, and the clean period.



496

497

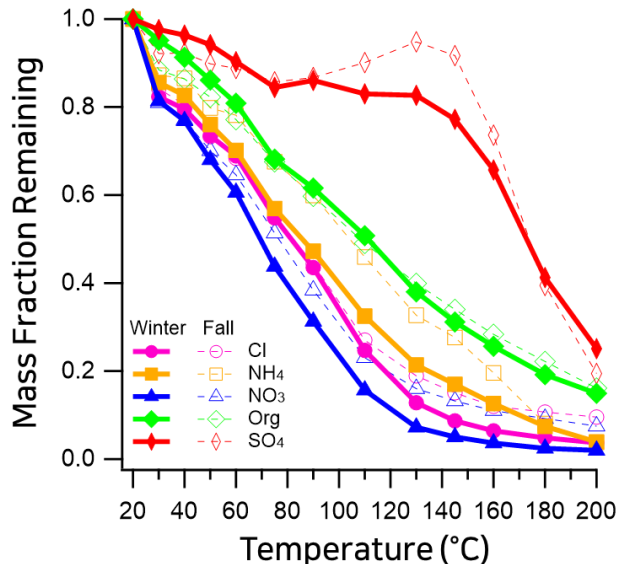
498 **Figure 2.** (a) Diurnal mean profiles of NOA and BBOA. Whiskers denote the 90th and 10th percentiles; box  
 499 edges represent the 75th and 25th percentiles; the horizontal line indicates the median, and the colored marker  
 500 shows the mean. The diurnal correlation between NOA and BBOA mean values is 0.63.  
 501 (b) Relative humidity (RH)-binned nighttime (19:00–05:00) profile of NOA. Box and whisker definitions are the  
 502 same as in panel (a). (c) Time series of NOA, BBOA, and amine-related ions ( $\text{CH}_4\text{N}^+$ ,  $\text{C}_2\text{H}_6\text{N}^+$ ,  $\text{C}_3\text{H}_8\text{N}^+$ ,  
 503  $\text{C}_5\text{H}_{12}\text{N}^+$ ), along with their correlations with NOA and BBOA.



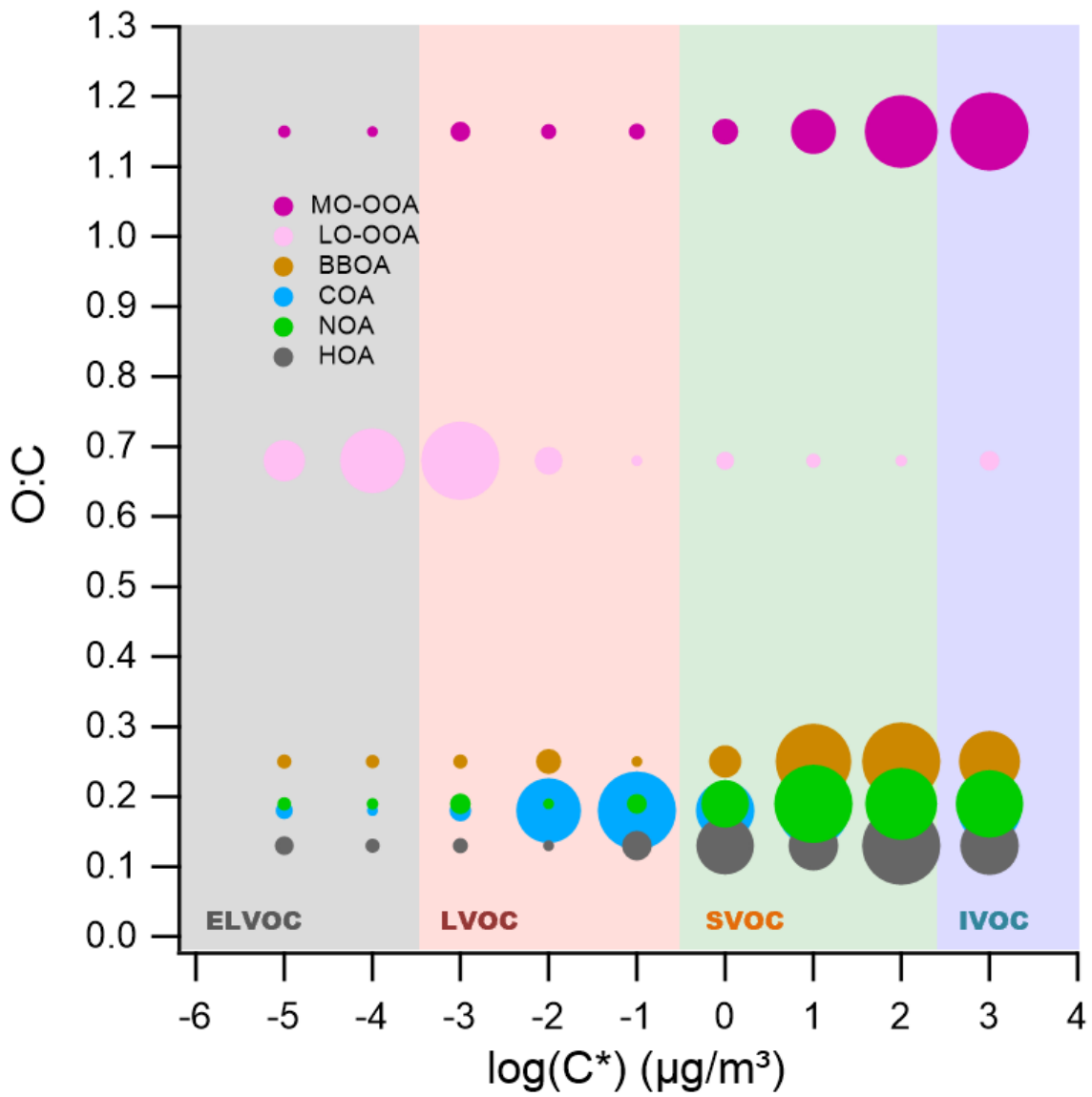
504

505

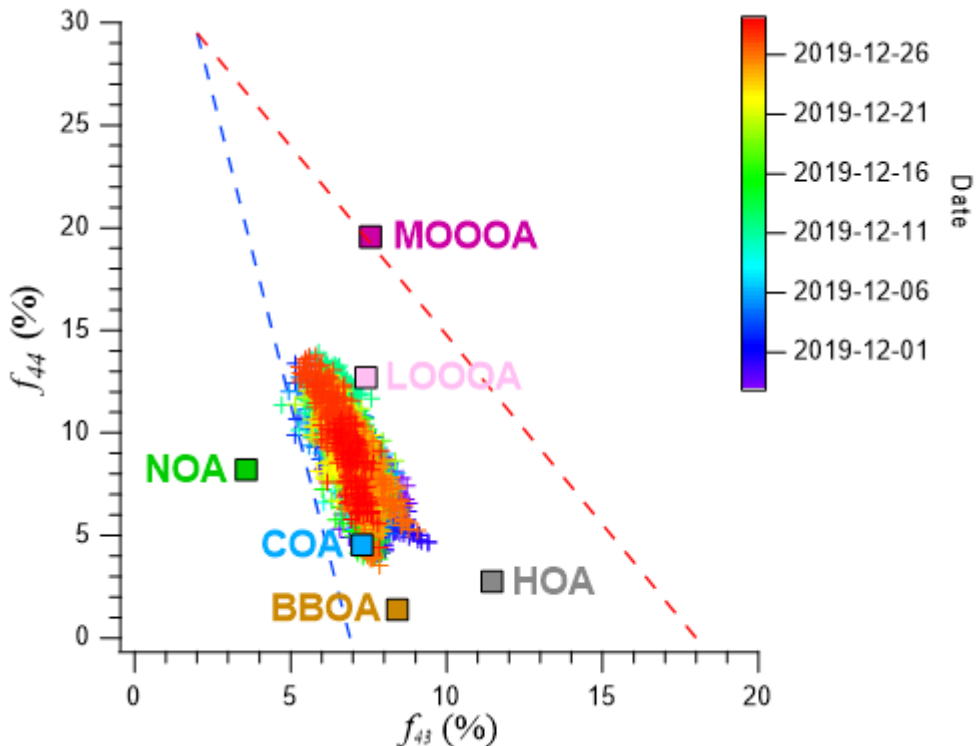
Figure 3. Mass spectra of (a) the NOA factor resolved by PMF analysis in this study, and reference spectra of amines from the NIST library: (b) dibutylamine (DBA), (c) dimethylamine (DMA), (d) methylamine (MA), and (e) trimethylamine (TMA). In panels (b)–(e), the left y-axis indicates the contribution of CHN-containing ions in the NOA factor (% of total), while the right y-axis shows the relative intensity of each compound's mass spectrum from the NIST library.



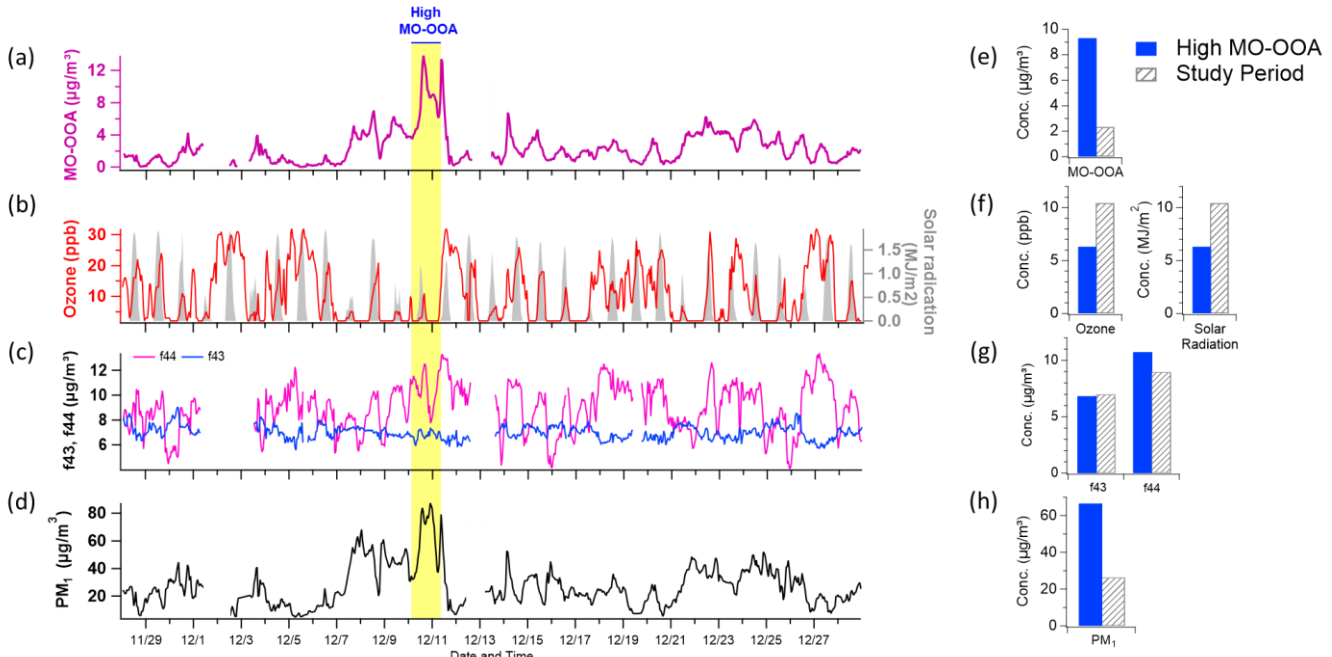
509 **Figure 4.** Mass fraction remaining (MFR) of non-refractory (NR) aerosol species measured in Seoul using a thermodenuder  
 510 coupled to a high-resolution time-of-flight aerosol mass spectrometer (HR-ToF-AMS). Winter 2019 (this study; dashed) is  
 511 compared with fall 2019 (previously reported; solid) (Jeon et al., 2023). Species include organics (magenta), nitrate (blue),  
 512 sulfate (orange), ammonium (green), and chloride (red).



513 **Figure 5.** Two-dimensional volatility basis set (2D-VBS) representation of organic aerosol (OA) sources identified in winter  
 514 2019 in Seoul. The plot illustrates the relationship between the oxygen-to-carbon (O:C) ratio and the effective saturation  
 515 concentration ( $C^*$ ) for each OA source resolved via positive matrix factorization (PMF). Solid circles represent the volatility  
 516 distribution across  $C^*$  bins, with marker size proportional to the mass fraction within each bin for the given source. Shaded  
 517 regions correspond to different volatility classes: extremely low-volatility organic compounds (ELVOCs), low-volatility  
 518 organic compounds (LVOCs), semi-volatile organic compounds (SVOCs), and intermediate-volatility organic compounds  
 519 (IVOCs), delineated by their  $C^*$  values.  
 520



521 **Figure 6.** scatterplot of  $f_{44}$  (CO<sub>2</sub><sup>+</sup>) versus  $f_{43}$  (C<sub>2</sub>H<sub>3</sub>O<sup>+</sup>). for the measured organic aerosol. The data points are color-coded by  
522 date to illustrate the temporal variation in OA composition throughout the observation period. The separated OA factors  
523 (HOA, COA, BBOA, NOA, LO-OOA, and MO-OOA) are also shown to enable comparison of source contributions and  
524 oxidation characteristics. The dashed line represents the typical  $f_{60}$  threshold associated with biomass-burning influence,  
525 while the triangular boundary indicates the conventional oxidative aging trend in the  $f_{44}$ – $f_{60}$  space.  
526



527  
528 **Figure 7.** Time series plots of (a) MO-OOA concentration, (b) ozone ( $\text{O}_3$ ) and solar radiation, (c)  $f_{44}$  and  $f_{43}$  (indicative of  
529 oxidation state), and (d) total  $\text{PM}_1$  concentration. The period characterized by elevated MO-OOA levels is highlighted in bright  
530 yellow. Panels (e)–(f) present comparative distributions of these variables—MO-OOA,  $\text{O}_3$  and solar radiation,  $f_{44}$  and  $f_{43}$ , and  
531  $\text{PM}_1$ —between the high MO-OOA period (shaded in blue) and the entire measurement period (indicated by gray hatching).  
532

533 **References**

534 Ghim, Y. S., Moon, K.-C., Lee, S., Kim, Y. P., 2005. Visibility trends in Korea during the past two decades. *J. Air*  
535 *Waste Manag. Assoc.* 55, 73–82. <https://doi.org/10.1080/10473289.2005.10464599>

536 Zhao, H., Che, H., Zhang, X., Ma, Y., Wang, Y., Wang, H., Wang, Y., 2013. Characteristics of visibility and  
537 particulate matter (PM) in an urban area of Northeast China. *Atmos. Pollut. Res.* 4, 427–434.  
538 <https://doi.org/10.5094/APR.2013.049>

539 Hamanaka, R. B., Mutlu, G. M., 2018. Particulate matter air pollution: Effects on the cardiovascular system. *Front.*  
540 *Endocrinol.* 9, 680. <https://doi.org/10.3389/fendo.2018.00680>

541 Manisalidis, I., Stavropoulou, E., Starvropoulos, A., Bezirtzoglou, E., 2020. Environmental and health impacts of  
542 air pollution: a review. *Front. Public Health* 8, 14. <https://doi.org/10.3389/fpubh.2020.00014>

543 IPCC, 2021. Climate Change 2021: The Physical Science Basis. Contribution of Working Group I to the Sixth  
544 Assessment Report of the Intergovernmental Panel on Climate Change, edited by Masson-Delmotte, V., Zhai,  
545 P., Pirani, A., Connors, S.L., Péan, C., Berger, S., et al. Cambridge University Press, Cambridge, UK and New  
546 York, NY, USA, pp. 817–922. <https://doi.org/10.1017/9781009157896.008>

547 Zhang, Q., Jimenez, J. L., Canagaratna, M. R., Allan, J. D., Coe, H., Ulbrich, I., Alfarra, M. R., Takami, A.,  
548 Middlebrook, A. M., Sun, Y. L., Dzepina, K., Dunlea, E., Docherty, K., DeCarlo, P., Salcedo, D., Onasch, T.  
549 B., Jayne, J. T., Miyoshi, T., Shimono, A., Hatakeyama, N., Takegawa, N., Kondo, Y., Schneider, J., Drewnick,  
550 F., Weimer, S., Demerjian, K. L., Williams, P. I., Bower, K. N., Bahreini, R., Cottrell, L., Griffin, R. J.,  
551 Rautianen, J., Worsnop, D. R., 2007. Ubiquity and dominance of oxygenated species in organic aerosols in  
552 anthropogenically-influenced Northern Hemisphere mid-latitudes. *Geophys. Res. Lett.* 34, L13801.  
553 <https://doi.org/10.1029/2007GL029979>

554 Jimenez, J. L., Canagaratna, M. R., Donahue, N. M., Prevot, A. S. H., Zhang, Q., Kroll, J. H., ... Worsnop, D. R.,  
555 2009. Evolution of organic aerosols in the atmosphere. *Science* 326, 1525–1529.  
556 <https://doi.org/10.1126/science.1180353>

557 Hallquist, M., Wenger, J. C., Baltensperger, U., Rudich, Y., Simpson, D., Claeys, M., ... Seinfeld, J. H., 2009. The  
558 formation, properties and impact of secondary organic aerosol: current and emerging issues. *Atmos. Chem.*  
559 *Phys.* 9, 5155–5236. <https://doi.org/10.5194/acp-9-5155-2009>

560 Robinson, A. L., Donahue, N. M., Shrivastava, M. K., Weitkamp, E. A., Sage, A. M., Grieshop, A. P., Lane, T. E.,  
561 Pierce, J. R., Pandis, S. N., 2007. Rethinking organic aerosols: Semivolatile emissions and photochemical aging.  
562 *Science* 315, 1259–1262. <https://doi.org/10.1126/science.1133061>

563 Donahue, N. M., Robinson, A. L., Stanier, C. O., Pandis, S. N., 2006. Coupled partitioning, dilution, and chemical  
564 aging of semivolatile organics. *Environ. Sci. Technol.* 40, 2635–2643. <https://doi.org/10.1021/es052297c>

565 Ng, N. L., Canagaratna, M. R., Zhang, Q., Jimenez, J. L., Tian, J., Ulbrich, I. M., Kroll, J. H., Docherty, K. S.,  
566 Chhabra, P. S., Bahreini, R., Murphy, S. M., Seinfeld, J. H., Hildebrandt, L., Donahue, N. M., DeCarlo, P. F.,  
567 Lanz, V. A., Prévôt, A. S. H., Dinar, E., Rudich, Y., Worsnop, D. R., 2010. Organic aerosol components  
568 observed in Northern Hemispheric datasets from Aerosol Mass Spectrometry. *Atmos. Chem. Phys.* 10, 4625–  
569 4641. <https://doi.org/10.5194/acp-10-4625-2010>

570 Cappa, C. D., Jimenez, J. L., 2010. Quantitative estimates of the volatility of ambient organic aerosol. *Atmos.*  
571 *Chem. Phys.* 10, 5409–5424. <https://doi.org/10.5194/acp-10-5409-2010>

572 Sinha, A., George, I., Holder, A., Preston, W., Hays, M., Grieshop, A. P., 2023. Development of volatility  
573 distributions for organic matter in biomass burning emissions. *Environ. Sci. Adv.* 3, 11–23.  
574 <https://doi.org/10.1039/D2EA00080F>

575 Glasius, M., Goldstein, A. H., 2016. Recent discoveries and future challenges in atmospheric organic chemistry.  
576 *Environ. Sci. Technol.* 50, 2754–2764. <https://doi.org/10.1021/acs.est.5b05105>

577 Matsui, H., Koike, M., Takegawa, N., Kondo, Y., Griffin, R. J., Miyazaki, Y., Yokouchi, Y., Ohara, T., 2009.  
578 Secondary organic aerosol formation in urban air: Temporal variations and possible contributions from  
579 unidentified hydrocarbons. *J. Geophys. Res. Atmos.* 114, D02209. <https://doi.org/10.1029/2008JD010164>

580 Jiang, F., Liu, Q., Huang, X., Wang, T., Zhuang, B., Xie, M., 2012. Regional modelling of secondary organic  
581 aerosol over China using WRF/Chem. *J. Aerosol Sci.* 53, 50–61. <https://doi.org/10.1016/j.jaerosci.2011.09.003>

582 Li, J., Zhang, M., Wu, F., Sun, Y., Tang, G., 2017. Assessment of the impacts of aromatic VOC emissions and  
583 yields of SOA on SOA concentrations with the air quality model RAMS-CMAQ. *Atmos. Environ.* 158, 105–  
584 115. <https://doi.org/10.1016/j.atmosenv.2017.03.035>

585 Zhao, B., Wang, S., Donahue, N. M., Jathar, S. H., Huang, X., Wu, W., ... & Hao, J. (2016). Quantifying the effect  
586 of organic aerosol aging and intermediate-volatility emissions on regional-scale aerosol pollution in China.  
587 *Scientific Reports*, 6, 28815. <https://doi.org/10.1038/srep28815>

588 Kang, H. G., Kim, Y., Collier, S., Zhang, Q., Kim, H., 2022. Volatility of springtime ambient organic aerosol  
589 derived with thermodenuder aerosol mass spectrometry in Seoul, Korea. *Environ. Pollut.* 310, 119203.  
590 <https://doi.org/10.1016/j.envpol.2022.119203>

591 Huang, X.-F., He, L.-Y., Hu, M., Canagaratna, M. R., Sun, Y., Zhang, Q., Worsnop, D. R., 2010. Highly time-  
592 resolved chemical characterization of atmospheric submicron particles during 2008 Beijing Olympic Games

593 using an Aerodyne High-Resolution Aerosol Mass Spectrometer. *Atmos. Chem. Phys.* 10, 8933–8945.  
594 <https://doi.org/10.5194/acp-10-8933-2010>

595 Mohr, C., DeCarlo, P. F., Heringa, M. F., Chirico, R., Slowik, J. G., Richter, R., Reche, C., Alastuey, A., Querol,  
596 X., Seco, R., Peñuelas, J., Jiménez, J. L., Crippa, M., Zimmermann, R., Baltensperger, U., Prévôt, A. S. H.,  
597 2012. Identification and quantification of organic aerosol from cooking and other sources in Barcelona using  
598 aerosol mass spectrometer data. *Atmos. Chem. Phys.* 12, 1649–1665. <https://doi.org/10.5194/acp-12-1649-2012>

600 Xu, L., Kollman, M. S., Song, C., Shilling, J. E., Ng, N. L., 2014. Effects of NO<sub>x</sub> on the volatility of secondary  
601 organic aerosol from isoprene photooxidation. *Environ. Sci. Technol.* 48, 2253–2262.  
602 <https://doi.org/10.1021/es404842g>

603 Grieshop, A. P., Logue, J. M., Donahue, N. M., Robinson, A. L., 2009. Laboratory investigation of photochemical  
604 oxidation of organic aerosol from wood fires 1: Measurement and simulation of organic aerosol evolution.  
605 *Atmos. Chem. Phys.* 9, 1263–1277. <https://doi.org/10.5194/acp-9-1263-2009>

606 Kim, H., Zhang, Q., Bae, G.-N., Kim, J.Y., Lee, S.B., 2017. Sources and atmospheric processing of winter aerosols  
607 in Seoul, Korea: Insights from real-time measurements using a high-resolution aerosol mass spectrometer.  
608 *Atmos. Chem. Phys.* 17, 2009–2033. <https://doi.org/10.5194/acp-17-2009-2017>

609 DeCarlo, P. F., Kimmel, J. R., Trimborn, A., Northway, M. J., Jayne, A. E., Aiken, A. C., ... & Jimenez, J. L.  
610 (2006). Field-deployable, high-resolution, time-of-flight aerosol mass spectrometer. *Analytical Chemistry*,  
611 78(24), 8281–8289. <https://doi.org/10.1021/ac061249>

612 Canagaratna, M. R., Jimenez, J. L., Kroll, J. H., Chen, Q., Kessler, S. H., Massoli, P., ... & Worsnop, D. R. (2015).  
613 Elemental ratio measurements of organic compounds using aerosol mass spectrometry: Improved sensitivity  
614 and intercomparability. *Atmospheric Chemistry and Physics*, 15(1), 253–272. <https://doi.org/10.5194/acp-15-253-2015>

616 Paatero, P., Tapper, U., 1994. Positive matrix factorization – A nonnegative factor model with optimal utilization  
617 of error estimates of data values. *Environmetrics* 5, 111–126. <https://doi.org/10.1002/env.3170050203>

618 Ulbrich, I. M., Canagaratna, M. R., Zhang, Q., Worsnop, D. R., Jimenez, J. L., 2009. Interpretation of organic  
619 components from Positive Matrix Factorization of aerosol mass spectrometric data. *Atmos. Chem. Phys.* 9,  
620 2891–2918. <https://doi.org/10.5194/acp-9-2891-2009>

621 Zhang, Q., Jimenez, J. L., Canagaratna, M. R., Ulbrich, I. M., Ng, N. L., Worsnop, D. R., Sun, Y., 2011.  
622 Understanding atmospheric organic aerosols via factor analysis of aerosol mass spectrometry: A review. *Anal.  
623 Bioanal. Chem.* 401, 3045–3067. <https://doi.org/10.1007/s00216-011-5355-y>

624 Huffman, J. A., Docherty, K. S., Aiken, A. C., Cubison, M. J., Ulbrich, I. M., DeCarlo, P. F., Jimenez, J. L., 2009.  
625 Chemically-resolved aerosol volatility measurements from two megacity field studies. *Atmos. Chem. Phys.* 9,  
626 7161–7182. <https://doi.org/10.5194/acp-9-7161-2009>

627 Saha, P. K., Khlystov, A., Grieshop, A. P., 2014. Determining aerosol volatility parameters using a “dual  
628 thermodenuder” system: Application to laboratory-generated organic aerosols. *Aerosol Sci. Technol.* 49, 620–  
629 632. <https://doi.org/10.1080/02786826.2015.1056769>

630 Zhou, S., Collier, S., Jaffe, D. A., Briggs, N. L., Hee, J., Sedlacek III, A. J., Kleinman, L., & Lewis, K., 2017.  
631 Regional influence of wildfires on aerosol chemistry in the western US and insights into atmospheric aging of  
632 biomass burning organic aerosol. *Atmospheric Chemistry and Physics*, 17, 2477–2493.  
633 <https://doi.org/10.5194/acp-17-2477-2017>

634 Riipinen, I., Pierce, J. R., Donahue, N. M., Pandis, S. N., 2010. Equilibration time scales of organic aerosol inside  
635 thermodenuders: Kinetics versus equilibrium thermodynamics. *Atmos. Environ.* 44, 597–607.  
636 <https://doi.org/10.1016/j.atmosenv.2009.11.022>

637 Karnezi, E., Riipinen, I., Pandis, S. N., 2014. Measuring the atmospheric organic aerosol volatility distribution: a  
638 theoretical analysis. *Atmos. Meas. Tech.* 7, 2953–2965. <https://doi.org/10.5194/amt-7-2953-2014>

639 Chen, Y., Wang, Z., Wang, Y., Zheng, X., Fu, P., Kawamura, K., Zhang, Y., 2021. Characterization of nitrogen-  
640 containing organic aerosol in Guangzhou, China: seasonal variation, formation mechanism and source  
641 apportionment. *Atmos. Chem. Phys.* 21, 4329–4344. <https://doi.org/10.5194/acp-21-4329-2021>

642 Hayes, P. L., Ortega, A. M., Cubison, M. J., Froyd, K. D., Zhao, Y., Cliff, S. S., ... Jimenez, J. L., 2013. Organic  
643 aerosol composition and sources in Pasadena, California, during the 2010 CalNex campaign. *J. Geophys. Res.*  
644 *Atmos.* 118, 9233–9257. <https://doi.org/10.1002/jgrd.50530>

645 Sun, Y., Jiang, Q., Wang, Z., Fu, P., Li, J., Yang, T., Yin, Y., 2011. Investigation of the sources and evolution  
646 processes of severe haze pollution in Beijing in January 2013. *J. Geophys. Res. Atmos.* 119, 4380–4398.  
647 <https://doi.org/10.1002/2014JD021641>

648 Baek, K. M., Park, E. H., Kang, H., Ji, M. J., Park, H. M., Heo, J & Kim, H., 2022. Seasonal characteristics of  
649 atmospheric water-soluble organic nitrogen in PM2.5 in Seoul, Korea: Source and atmospheric processes of  
650 free amino acids and aliphatic amines. *Science of the Total Environment*, 807, 150785.  
651 <https://doi.org/10.1016/j.scitotenv.2021.152335>

652 Rovelli, G., Miles, R. E. H., Reid, J. P., and Clegg, S. L.: Hygroscopic properties of aminium sulfate aerosols,  
653 *Atmos. Chem. Phys.*, 17, 4369–4385, <https://doi.org/10.5194/acp-17-4369-2017>, 2017.

654 Ge, X., Wexler, A. S., Clegg, S. L., 2011. Atmospheric amines – Part I. A review. *Atmos. Environ.* 45, 524–546.  
655 <https://doi.org/10.1016/j.atmosenv.2010.10.012>

656 He, L.-Y., Lin, Y., Huang, X. F., Guo, W. W., Niu, J. L., Shen, Y. F., Sen, J., and Hu, M.: Characterization of high-  
657 resolution aerosol mass spectra of primary organic aerosol emissions from Chinese cooking and biomass  
658 burning, *Atmos. Chem. Phys.*, 10, 11535–11543, <https://doi.org/10.5194/acp-10-11535-2010>, 2010

659 You, Y., Renbaum-Wolff, L., Carreras-Sospedra, M., Dabdub, D., Bertram, A. K., Martin, S. T., et al., 2014.  
660 Images reveal that amines promote the heterogeneous reaction of epoxides in model organic aerosols. *J. Phys.*  
661 *Chem. Lett.* 5, 3211–3215. <https://doi.org/10.1021/jz501268k>

662 Yao, L., Wang, M. Y., Wang, X. K., Zhang, W. Q., Liu, Y., Li, L., et al., 2016. Atmospheric new particle formation  
663 from sulfuric acid and amines in a Chinese megacity. *Sci. Bull.* 61, 939–945. <https://doi.org/10.1007/s11434-016-1083-0>

664 Kim, H., Zhang, Q., Sun, Y., Bae, G. N., Lee, B. E., Park, K., ... & Kim, Y. J. 2020. Measurement report:  
665 Characterization of severe spring haze episodes and influences of long-range transport in the Seoul  
666 metropolitan area in March 2019. *Atmospheric Chemistry and Physics*, 20(18), 11527–11545.  
667 <https://doi.org/10.5194/acp-20-11527-2020>

668 Jeon, J., Chen, Y., Kim, H., 2023. Influence of meteorology on emission sources and physicochemical properties  
669 of particulate matter in Seoul, Korea during heating period. *Atmos. Environ.* 301, 119733.  
670 <https://doi.org/10.1016/j.atmosenv.2023.119733>

671 Zhang, Q., Alfarra, M. R., Worsnop, D. R., Allan, J. D., Coe, H., Canagaratna, M. R., ... & Jimenez, J. L. 2005.  
672 Deconvolution and quantification of hydrocarbon-like and oxygenated organic aerosols based on aerosol mass  
673 spectrometry. *Environmental Science & Technology*, 39(13), 4938–4952. <https://doi.org/10.1021/es0485681>

674 Simoneit, B. R. T. 2002. Biomass burning – a review of organic tracers for smoke from incomplete combustion.  
675 *Applied Geochemistry*, 17(3), 129–162. [https://doi.org/10.1016/S0883-2927\(01\)00061-0](https://doi.org/10.1016/S0883-2927(01)00061-0)

676 Cubison, M. J., Ortega, A. M., Hayes, P. L., Farmer, D. K., Day, D., Lechner, M. J., ... & Jimenez, J. L. 2011.  
677 Effects of aging on organic aerosol from open biomass burning smoke in aircraft and laboratory studies.  
678 *Atmospheric Chemistry and Physics*, 11(23), 12049–12064. <https://doi.org/10.5194/acp-11-12049-2011>

679 Xu, L., Williams, L. R., Young, D. E., Allan, J. D., Coe, H., Massoli, P., Fortner, E., Chhabra, P., Herndon, S.,  
680 Brooks, W. A., Jayne, J. T., Worsnop, D. R., Aiken, A. C., Liu, S., Gorkowski, K., Dubey, M. K., Fleming, Z.  
681 L., Visser, S., Prévôt, A. S. H., Ng, N. L., 2016. Wintertime aerosol chemical composition, volatility, and  
682 spatial variability in the Greater London Area. *Atmos. Chem. Phys.* 16, 1139–1160.  
683 <https://doi.org/10.5194/acp-16-1139-2016>

684

685 Feng, T., Wang, Y., Hu, W., Zhu, M., Song, W., Chen, W., ... Wang, X., 2023. Impact of aging on the sources,  
686 volatility, and viscosity of organic aerosols in Chinese outflows. *Atmos. Chem. Phys.* 23, 611–636.  
687 <https://doi.org/10.5194/acp-23-611-2023>

688 Scott, W. D., & Cattell, F. C. R. 1979. Vapor pressure of ammonium sulfates. *Atmospheric Environment* (1967),  
689 13(6), 987–1000. [https://doi.org/10.1016/0004-6981\(79\)90174-4](https://doi.org/10.1016/0004-6981(79)90174-4)

690 Donahue, N. M., Robinson, A. L., Pandis, S. N., 2009. Atmospheric organic particulate matter: From smoke to  
691 secondary organic aerosol. *Atmos. Environ.* 43, 94–106. <https://doi.org/10.1016/j.atmosenv.2008.09.055>

692 Ehn, M., Thornton, J. A., Kleist, E., Sipilä, M., Junninen, H., Pullinen, I., ... & Kulmala, M. 2014. A large source  
693 of low-volatility secondary organic aerosol. *Nature*, 506(7489), 476–479. <https://doi.org/10.1038/nature13032>

694 Kroll, J. H., Smith, J. D., Che, D. L., Kessler, S. H., Worsnop, D. R., Wilson, K. R., 2009. Measurement of  
695 fragmentation and functionalization pathways in the heterogeneous oxidation of oxidation organic aerosol.  
696 *Environ. Sci. Technol.* 43, 7826–7833. <https://doi.org/10.1021/es901683r>

697 Xu, W., Takeuchi, M., Chen, C., Qiu, Y., Xie, C., Xu, W., Ma, N., Worsnop, D. R., Ng, N. L., and Sun, Y.:  
698 Estimation of particulate organic nitrates from thermodenuder–aerosol mass spectrometer measurements in  
699 the North China Plain, 14, 3693–3705, <https://doi.org/10.5194/amt-14-3693-2021>, 2021.

700 Cao, L.-M., Huang, X.-F., Li, Y.-Y., Hu, M., He, L.-Y., 2018. Volatility measurement of atmospheric submicron  
701 aerosols in an urban atmosphere in southern China. *Atmos. Chem. Phys.* 18, 1729–1743.  
702 <https://doi.org/10.5194/acp-18-1729-2018>

703 Xu, W., Xie, C., Karnezi, E., Zhang, Q., Wang, J., Pandis, S.N., Ge, X., Zhang, J., An, J., Wang, Q., et al., 2019.  
704 Summertime aerosol volatility measurements in Beijing, China. *Atmos. Chem. Phys.* 19, 10205–10216.  
705 <https://doi.org/10.5194/acp-19-10205-2019>

706 Allan, J. D., Alfarra, M. R., Bower, K. N., Williams, P. I., Gallagher, M. W., Jimenez, J. L., McDonald, A. G.,  
707 Nemitz, E., Canagaratna, M. R., and Coe, H.: Quantitative sampling using an Aerodyne aerosol mass  
708 spectrometer—2. Measurements of fine particulate chemical composition in two U.K. cities, *J. Geophys. Res.-*  
709 *Atmos.*, 108, 4091, 2003, <https://doi.org/10.1029/2002JD002359>.

710 Berndt, T., Richters, S., Jokinen, T., et al.: Hydroxyl radical-induced formation of highly oxidized organic  
711 compounds, *Nat. Commun.*, 7, 13677, 2016, <https://doi.org/10.1038/ncomms13677>.

712 Bianchi, F., Kurtén, T., Riva, M., et al.: Highly oxygenated organic molecules (HOM) from gas-phase autoxidation  
713 involving peroxy radicals: A key contributor to atmospheric aerosol, *Chem. Rev.*, 119, 3472–3509, 2019,  
714 <https://doi.org/10.1021/acs.chemrev.8b00395>.

715 Brown, S. S. and Stutz, J.: Nighttime radical observations and chemistry, *Chem. Soc. Rev.*, 41, 6405–6447, 2012,  
716 <https://doi.org/10.1039/C2CS35181A>.

717 Canagaratna, M. R., Jayne, J. T., Jimenez, J. L., et al.: Chemical and microphysical characterization of ambient  
718 aerosols with the Aerodyne aerosol mass spectrometer, *Mass Spectrom. Rev.*, 26, 185–222, 2007,  
719 <https://doi.org/10.1002/mas.20115>.

720 Chhabra, P. S., Ng, N. L., Canagaratna, M. R., et al.: Elemental composition and oxidation of chamber organic  
721 aerosol, *Atmos. Chem. Phys.*, 11, 8827–8841, 2011, <https://doi.org/10.5194/acp-11-8827-2011>.

722 D'Ambro, E. L., Schobesberger, S., Gaston, C. J., et al.: Molecular composition and volatility of isoprene  
723 photochemical oxidation secondary organic aerosol under low- and high-NO<sub>x</sub> conditions, *Atmos. Chem. Phys.*,  
724 17, 159–174, 2017, <https://doi.org/10.5194/acp-17-159-2017>.

725 Donahue, N. M., Epstein, S. A., Pandis, S. N., and Robinson, A. L.: A two-dimensional volatility basis set – Part  
726 1: Organic-aerosol mixing thermodynamics, *Atmos. Chem. Phys.*, 11, 3303–3318, 2011,  
727 <https://doi.org/10.5194/acp-11-3303-2011>.

728 Faulhaber, A. E., Thomas, B. M., Jimenez, J. L., et al.: Characterization of a thermodenuder–particle beam mass  
729 spectrometer system for the study of organic aerosol volatility and composition, *Atmos. Meas. Tech.*, 2, 15–  
730 31, 2009, <https://doi.org/10.5194/amt-2-15-2009>.

731 Ge, X., Wexler, A. S., and Clegg, S. L.: Atmospheric amines – Part III: Photochemistry and toxicity, *Atmos.*  
732 *Environ.*, 45, 561–591, 2011, <https://doi.org/10.1016/j.atmosenv.2010.11.050>.

733 Gil, J., Lee, Y., and Kim, Y. P.: Characteristics of HONO and its impact on O<sub>3</sub> formation in the Seoul Metropolitan  
734 Area during KORUS-AQ, *Atmos. Environ.*, 246, 118032, 2021,  
735 <https://doi.org/10.1016/j.atmosenv.2020.118032>.

736 Han, K.-M., Kim, D.-G., Kim, J., et al.: Crop residue burning emissions and impact on particulate matter over  
737 South Korea, *Atmosphere*, 13, 559, 2022, <https://doi.org/10.3390/atmos13040559>.

738 Hanson, D. R., McMurry, P. H., Jiang, J., et al.: Ambient pressure proton transfer mass spectrometry: detection of  
739 amines and ammonia, *Environ. Sci. Technol.*, 45, 8881–8888, 2011, <https://doi.org/10.1021/es2018817>.

740 Hennigan, C. J., Sullivan, A. P., Collett, J. L., Jr., and Robinson, A. L.: Levoglucosan stability in biomass burning  
741 particles exposed to hydroxyl radicals, *Geophys. Res. Lett.*, 37, L09806, 2010,  
742 <https://doi.org/10.1029/2010GL043088>.

743 Huffman, J. A., Ziemann, P. J., Jayne, J. T., et al.: Development and characterization of a fast-stepping  
744 thermodenuder for chemically resolved aerosol volatility measurements, *Aerosol Sci. Technol.*, 42, 395–407,  
745 2008, <https://doi.org/10.1080/02786820802104981>.

746 Kim, K., Park, R., Lee, Y., et al.: An investigation into atmospheric nitrous acid (HONO) and its sources in East  
747 Asia, *Atmos. Chem. Phys.*, 24, 12575–12593, 2024, <https://doi.org/10.5194/acp-24-12575-2024>.

748 Kroll, J. H. and Seinfeld, J. H.: Chemistry of secondary organic aerosol: Formation and evolution of low-volatility  
749 organics in the atmosphere, *Atmos. Environ.*, 42, 3593–3624, 2008,  
750 <https://doi.org/10.1016/j.atmosenv.2008.01.003>.

751 Kroll, J., Donahue, N., Jimenez, J., et al.: Carbon oxidation state as a metric for describing the chemistry of  
752 atmospheric organic aerosol, *Nat. Chem.*, 3, 133–139, 2011, <https://doi.org/10.1038/nchem.948>.

753 Kwon, S., Won, S. R., Lim, H. B., et al.: Relationship between PM1.0 and PM2.5 in urban and background areas  
754 of the Republic of Korea, *Atmos. Pollut. Res.*, 14, 101858, 2023, <https://doi.org/10.1016/j.apr.2023.101858>.

755 Lamb, K. D., Kim, B.-G., and Kim, S.-W.: Estimating source-region influences on black carbon in South Korea  
756 using the BC/CO ratio, *J. Geophys. Res.-Atmos.*, 123, 11, 2018, <https://doi.org/10.1029/2018JD029257>.

757 Lambe, A. T., Onasch, T. B., Massoli, P., et al.: Transitions from Functionalization to Fragmentation Reactions of  
758 Laboratory Secondary Organic Aerosol (SOA) Generated from the OH Oxidation of Alkane Precursors,  
759 *Environ. Sci. Technol.*, 46, 5430–5437, 2012, <https://doi.org/10.1021/es300274t>.

760 López-Hilfiker, F. D., Mohr, C., Ehn, M., et al.: A novel method for online analysis of gas and particle composition:  
761 description and evaluation of a Filter Inlet for Gases and AEROSols (FIGAERO), *Atmos. Meas. Tech.*, 7, 983–  
762 1001, 2014, <https://doi.org/10.5194/amt-7-983-2014>.

763 López-Hilfiker, F. D., Mohr, C., Ehn, M., et al.: Molecular composition and volatility of organic aerosol in the  
764 Southeastern U.S. using FIGAERO–CIMS with comparison to AMS, *Environ. Sci. Technol.*, 50, 2200–2209,  
765 2016, <https://doi.org/10.1021/acs.est.5b04769>.

766 Mao, J., Wang, L., Lu, C., et al.: High-resolution modeling of gaseous methylamines over a polluted region in  
767 China: source-dependent emissions and implications of spatial variations, *Atmos. Chem. Phys.*, 18, 7933–7950,  
768 2018, <https://doi.org/10.5194/acp-18-7933-2018>.

769 Matsui, H., Koike, M., Kondo, Y., et al.: An estimation of the organic aerosol component in PM2.5 using AMS  
770 and CMB models, *J. Geophys. Res.-Atmos.*, 114, D21203, 2009, <https://doi.org/10.1029/2009JD012170>.

771 Nault, B. A., Campuzano-Jost, P., Day, D. A., et al.: Secondary organic aerosol production from local emissions  
772 dominates over Seoul during KORUS-AQ, *Atmos. Chem. Phys.*, 18, 17769–17800, 2018,  
773 <https://doi.org/10.5194/acp-18-17769-2018>.

774 Nielsen, C. J., Herrmann, H., and Weller, C.: Atmospheric chemistry and environmental impact of the use of amines  
775 in carbon capture and storage (CCS), *Chem. Soc. Rev.*, 41, 6684–6704, 2012,  
776 <https://doi.org/10.1039/C2CS35059A>.

777 Slater, E. J., Gkatzoflias, D., Wang, Y., et al.: Elevated levels of OH observed in haze events during wintertime  
778 Beijing, *Atmos. Chem. Phys.*, 20, 14847–14871, 2020, <https://doi.org/10.5194/acp-20-14847-2020>.

779 Sun, Y., Zhang, Q., Schwab, J. J., et al.: Characterization of the sources and properties of organic aerosol from  
780 AMS measurements during a winter campaign in Beijing, China, *Atmos. Chem. Phys.*, 10, 8951–8971, 2010,  
781 <https://doi.org/10.5194/acp-10-8951-2010>.

782 Tiszenkel, L., Flynn, J. H., and Lee, S.-H.: Measurement report: Urban ammonia and amines in Houston, Texas,  
783 *Atmos. Chem. Phys.*, 24, 11351–11363, 2024, <https://doi.org/10.5194/acp-24-11351-2024>.

784 Yoo, H., Lee, H., and Kim, Y. P.: Insights from single-particle analysis: submicron aerosol composition in Seoul  
785 during KORUS-AQ, *Atmos. Chem. Phys.*, 24, 853–872, 2024, <https://doi.org/10.5194/acp-24-853-2024>.

786 Ziemann, P. J. and Atkinson, R.: Kinetics, products, and mechanisms of secondary organic aerosol formation from  
787 gas-phase reactions of organic compounds, *Chem. Soc. Rev.*, 41, 6582–6605, 2012,  
788 <https://doi.org/10.1039/C2CS35122F>.

789 Paciga, A., Young, D. E., Ward, M. W., et al.: Volatility of organic aerosol and its components in the megacity of  
790 Paris, *Atmos. Chem. Phys.*, 16, 2013–2031, 2016, <https://doi.org/10.5194/acp-16-2013-2016>.

791 Ge, X., Wexler, A. S., and Clegg, S. L.: Atmospheric amines – Part II. Thermodynamic properties and gas-particle  
792 partitioning, *Atmos. Chem. Phys.*, 11, 55–69, 2011, <https://doi.org/10.5194/acp-11-55-2011>.

793 Xu, W., Sun, Y., Wang, Q., et al.: Seasonal characterization of organic nitrogen in atmospheric aerosols using high-  
794 resolution aerosol mass spectrometry in Beijing, China, *ACS Earth Space Chem.*, 1, 649–658, 2017,  
795 <https://doi.org/10.1021/acsearthspacechem.7b00106>.

796 Sun, Y. L., Zhang, Q., Schwab, J. J., et al.: Characterization of the sources and processes of organic and inorganic  
797 aerosols in New York City with a high-resolution time-of-flight aerosol mass spectrometer, *Atmos. Chem.*  
798 *Phys.*, 11, 1581–1602, 2011, <https://doi.org/10.5194/acp-11-1581-2011>.

799 Saarikoski, S., Carbone, S., Decesari, S., et al.: Chemical characterization of springtime submicrometer aerosol in  
800 Po Valley, Italy, *Atmos. Chem. Phys.*, 12, 8401–8421, 2012, <https://doi.org/10.5194/acp-12-8401-2012>.

801 Silva, P. J., Erupe, M. E., Price, D., et al.: Trimethylamine as precursor to secondary organic aerosol formation via  
802 nitrate radical reaction in the atmosphere, *Environ. Sci. Technol.*, 42, 4689–4696, 2008,  
803 <https://doi.org/10.1021/es703016v>

804 EPA: EPA Positive Matrix Factorization (PMF) 5.0 Fundamentals and User Guide, U.S. Environmental Protection  
805 Agency, 2014. [https://www.epa.gov/sites/default/files/2015-02/documents/pmf\\_5.0\\_user\\_guide.pdf](https://www.epa.gov/sites/default/files/2015-02/documents/pmf_5.0_user_guide.pdf)

806 Waked, A., Favez, O., Alleman, L.Y., Piot, C., Petit, J.E., Delaunay, T., Verlinden, E., Jayne, J., Sciare, J., 2014.  
807 Source apportionment of PM10 in a north-western Europe regional urban background site (Lens, France) using

808 positive matrix factorization and including primary emissions. *Atmos. Chem. Phys.* 14, 3325–3346.  
809 <https://doi.org/10.5194/acp-14-3325-2014>

810 Soleimani, M., Ebrahimi, Z., Mirghaffari, N., Naseri, M., 2022. Source identification of polycyclic aromatic  
811 hydrocarbons associated with fine particulate matters (PM2.5) in Isfahan City, Iran, using diagnostic ratio and  
812 PMF model. *Environ. Sci. Pollut. Res.* 29, 30310–30326. <https://doi.org/10.1007/s11356-021-17635-8>

813 Allan, J. D., Williams, P. I., Morgan, W. T., et al.: Contributions from transport, solid fuel burning and cooking to  
814 primary organic aerosols in two UK cities, *Atmos. Chem. Phys.*, 10, 647–668, 2010,  
815 <https://doi.org/10.5194/acp-10-647-2010>.

816 Mohr, C., DeCarlo, P. F., Heringa, M. F., et al.: Identification and quantification of organic aerosol from cooking  
817 and other sources in Barcelona using aerosol mass spectrometer data, *Atmos. Chem. Phys.*, 12, 1649–1665,  
818 2012, <https://doi.org/10.5194/acp-12-1649-2012>.

819 Sun, Y.-L., Zhang, Q., Schwab, J. J., et al.: Characterization of the sources and processes of organic aerosols in  
820 New York City with a high-resolution time-of-flight aerosol mass spectrometer, *Atmos. Chem. Phys.*, 11,  
821 1581–1602, 2011, <https://doi.org/10.5194/acp-11-1581-2011>.

822